Doctoral Thesis in Physics

Observations of nearby Galaxy Clusters with the Fermi Large Area Telescope

Towards the first Gamma Rays from Clusters

Stephan Zimmer

Oskar Klein Centre for Cosmoparticle Physics

and

Cosmology, Particle Astrophysics and String Theory

Department of Physics
Stockholm University
SE-106 91 Stockholm

Stockholm, Sweden 2015

Stockholm
University

Cover Image: False-Color image of the Coma cluster in γ-rays (red), X-rays (green) and radio (blue). X-ray images are taken from a mosaic of XMM Newton observations in the $2.0 - 7.2\,\mathrm{keV}$ band [Image Credit: S. Snowden NASA/GSFC XMM-Newton GOF]. The radio image was kindly provided by L. Rudnick and is taken at 352 MHz with the Westerbork Synthesis Radio Telescope [Image Credit: L. Rudnick]. Compact sources have been removed (though removal artifacts from Coma A are still present); image convolved with 135". The γ-ray observations are based on the TS-map taken from Paper IV. Note that the X-ray mosaic extend to at most 95' not spanning the same region as the radio and γ-ray counterparts.

ISBN 978-91-7649-270-3 (pp. i–xvi, 1–79)

Printed in Sweden by Holmbergs, Malmö 2015.
Distributor: Department of Physics, Stockholm University
Typeset in pdfLaTeX

Preface

Abstract

Galaxy clusters are the most massive bound systems known in the Universe and are believed to have formed through large scale structure formation. They host relativistic cosmic-ray (CR) populations and are gravitationally bound by large amounts of Dark Matter (DM), both providing conditions in which high-energy gamma rays may be produced either via CR interactions with the intracluster medium or through the annihilation or decay of DM particles.

Prior to the launch of the Fermi satellite, predictions were optimistic that these sources would be established as gamma-ray-bright objects by observations through its prime instrument, the Large Area Telescope (LAT). Yet, despite numerous efforts, even a single firm cluster detection is still pending. This thesis presents a number of studies based on data taken by the LAT over its now seven year mission aiming to discover these γ rays.

Using a joint likelihood technique, we study the γ-ray spectra of a sample of nearby clusters searching for a CR-induced signal due to hadronic interactions in the intracluster medium. While we find excesses in some individual targets, we attribute none to the cluster. Hence, we constrain the maximum injection efficiency of hadrons being accelerated in structure formation shocks and the fraction of CR-to-thermal pressure. We also perform a refined search targeting the Coma cluster specifically due to its large variety of existing observations in other wavebands. In the latter case we find weak indications of an excess which however falls below the detection threshold.

Because the cluster emission we consider is inherently extended, we need to take into account the imperfect modeling of the foreground emission, which may be particularly difficult such as is the case with the Virgo cluster. Here, we assess the systematics associated with the foreground uncertainties and derive limits based on an improved background model of the region. For the first time we derive limits on the γ-ray flux from CR and DM-interactions in which we take into account the dynamical state of the system. For DM we also include the contribution from substructure. The DM domain is further explored by searching for line-like features as they arise from the annihilation of DM into two photons in a large sample of clusters, including Virgo and Coma. Finding no evidence for γ-ray lines, we derive limits on the DM annihilation cross section that are roughly a factor 10 (100) above that derived from observations of the galactic center assuming an optimistic (conservative) scenario regarding the boost due to DM substructure.

Keywords: Galaxy Clusters, Fermi-LAT, γ rays, Dark Matter, Cosmic Rays

In memory of Wolfgang Pagel

List of Papers

The following papers, referred to in the text by their Roman numerals, are included in this thesis.

Paper I M. Ackermann, M. Ajello, A. Albert, *et al.* (The Fermi-LAT collaboration). *Search for Cosmic-Ray-induced Gamma-Ray Emission in Galaxy Clusters*,
ApJ **787**, 18 (2014)
DOI: doi:10.1088/0004-637X/787/1/18
arXiv: astro-ph/1308.5654.

Paper II M. Ackermann, M. Ajello, A. Albert, *et al.* (The Fermi-LAT collaboration). *Search for extended gamma-ray emission from the Virgo Galaxy Cluster with Fermi-LAT*,
ApJ*, in press*
arXiv: astro-ph/1510.00004.

Paper III B. Anderson, S. Zimmer, J. Conrad, M. Gustafsson, M. Sánchez-Conde, R. Caputo. *Search for gamma-ray lines towards Galaxy Clusters with the Fermi-LAT*,
in preparation .

Paper IV M. Ackermann, M. Ajello, A. Albert, *et al.* (The Fermi-LAT collaboration). *Search for gamma-ray emission from the Coma Cluster with six years of Fermi-LAT data*,
ApJ*, submitted*
arXiv: astro-ph/1507.08995.

Reprints were made with the permission of the publishers.

Complementary Papers not included in this thesis

Paper V S. Zimmer, J. Conrad and A. Pinzke, (for the Fermi-LAT collaboration). *A Combined Analysis of Clusters of Galaxies - Gamma Ray Emission from Cosmic Rays and Dark Matter*,
Contribution to the 2011 Fermi Symposium - eConf Proceedings C110509 (2011)
arXiv: astro-ph/1110.6863.

Paper VI S. Zimmer, L. Arrabito, T. Glanzman *et al.* (for the Fermi-LAT collaboration). *Extending the Fermi-LAT Data Processing Pipeline to the Grid*,
J. Phys.: Conf. Ser. **396**, 032121 (2012)
DOI: doi:10.1088/1742-6596/396/3/032121
arXiv: astro-ph/1212.4115.

Paper VII T. Jogler, S. Zimmer, S. Funk *et al.*, (for the Fermi-LAT collaboration). *Search for extended gamma-ray emission from the Virgo Galaxy Cluster with Fermi/LAT*,
In 33rd International Cosmic Ray Conference (ICRC), Rio De Janeiro 2013 (pp. 2 - 4) (2013)
`http://www.cbpf.br/~icrc2013/papers/icrc2013-0993.pdf`.

Paper VIII S. Zimmer (for the Fermi-LAT collaboration). *Galaxy Clusters with the Fermi-LAT: Status and Implications for Cosmic Rays and Dark Matter Physics,*
Contribution to the 2014 Fermi Symposium - eConf Proceedings C14102.1 (2014)
arxiv: astro-ph/1502.02653.

Contents

List of Figures

Acknowledgements

This thesis documents work that I have carried out over the period of five years. During this time I have crossed the paths of many whom I am indebted and who I wish to acknowledge.

First off, I extend my sincere gratitude to my advisor J. Conrad. His steady guidance has allowed me to pursue my own ideas while it was firm enough to not get me side-tracked. Aside from his sheer infinite patience with me, I also appreciate the open and no-nonsense attitude he employed during the past years in addition to the generosity of sending me off to many, many conferences without me having to worry too much about the financial side of things - several things I will be missing from now on.

Thanks to my co-advisor L. Bergström for sharing his anecdotes about the nobel prize and for having his door open whenever I needed his advice. I would also like to acknowledge the support of my mentor C. Finley who shared the neutrino perspective of clusters with me.

Next, I would like to thank my long term collaborators, A. Pinzke, O. Reimer and Y. Rephaeli for sharing their wisdom on cluster physics, non-thermal emission and for infecting me with the passion to hunt clusters in γ rays. Both M. Gustafsson and M. Sánchez-Conde are thanked for their great patience explaining the details of DM modeling, substructure discussions and for their invaluable contributions to the various papers and the projects we have worked together on. I owe B. Anderson more beer than I can count for the hard work that was required to get the line paper finally out the door. T. Jogler is thanked for shouldering the burden of the Virgo paper along with the various iterations it took to get in shape. Thanks to E. Ferrara for sharing some of the FSSC secrets, how to do variability analysis and for showing me how astronomers can have a good time at AAS meetings. I wish to extend my gratitude to the internal reviewers of my papers and their diligence when moving each paper towards journal submission: K. Bechtol (twice!), J. Chiang, G. Madejski, A. Strong, G. Gomez-Vargas, J. Gaskins and R. Caputo. S. Digel is thanked for his help in improving every single manuscript - be it proceedings or paper, up to the formatting of references.

My presence in the *Fermi* collaboration has made me felt welcome and appreciated, both which I am grateful for. During my time in the collaboration I was fortunate to enjoy the special atmosphere the Pass 8 "bubble" radiated. It was a pleasure to work alongside (and for) B. Atwood, L. Baldini & L. Latronico, P. Bruel, C. Sgro, T. Usher, L. Rochester, E. Charles & E. Grove, J. Cohen-Tanugi, & A. Drlica-Wagner (to name but

a few of the people that made Pass 8 a reality). Other *Fermi*ons whom I am especially grateful to are: M. Ajello, J. Ballet, E. Bloom, S. Ciprini, S. Cutini D. Gasparrini, J. Kataoka, M. Kuss, J. Lande, F. Longo, F. Piron, and R. Rando. I would not have been able to carry out some of my tasks if it weren't for R. Dubois and T. Glanzman who (despite me bringing the almighty SLAC computing farm to its knees more than once) continued to grant all my computing resource requests and who together with T. Johnson taught me the pesky internals of the Fermi data processing. I thank the DIRAC folks and affiliates for their continued help in getting the pipeline connection up in shape: S. Poss, A. Tsaregorodtsev, V. Hamar, L. Arrabito, S. Viscapi & V. Rolland. I also wish to acknowledge N. Bergvall who introduced me to cosmology and the Dark Matter problem. Without him I may still be hunting Higgs bosons instead.

I am grateful to Maja for her help during my first year and for her friendship that extends beyond the office. Thanks to my present (and former) office mates for spending that much time together: Knut (and thanks for watering the plants!), Calle, Hugh and Joachim. Aside from the already mentioned folks, I'd like to thank the Fermi group in Stockholm, including Manuel & Andrea for providing a fantastic work environment and for their advice (and patience) during our meetings, along to being great travel mates. Thanks to Regina, Fabio, Miguel, Knut, and Andrea for providing useful comments on the thesis manuscript.

Thanks to my fellow PhD-students and post-docs for making the OKC a great place to be: Tanja, Joel, Irina, Christian, Robert, Raphael, Ben, Emily, Timur, Angnis and everyone I might have missed in this list. Thanks to Ariel for introducing me to big-shots in the cluster field early on and to the whole CoPS group at Fysikum. I thank my brother-in-arms Mikke for sharing the hardship of fighting for students rights and past Ph.D. councils for their trust in our ability to lead them. Thanks to my roomies Marcel & Vlado for taking care of things while I was busy writing (or at a conference). I am grateful to my long time friends Simon, Martin and Andrea for dragging me out of the office every now and then and to Jerker and Sebastian for them continuing to ask the annoying questions while usually not being satisfied with my responses. Apologies to Florian for saying no maybe a tad too often and to Ilka for not joining her sailing adventures more frequently. I would also like to thank both Nils Bergvall, Rikard Enberg and Gunnar Ingelman: Nils for introducing me to the strange world of cosmology and the Dark Matter problem and Rikard and Gunnar for giving the right advice at the right time.

Ich danke meiner Familie, allen voran meinen Eltern, Claudia & Erhard für die Unterstützung (moralisch aber auch finanziell) ohne deren Hilfe ich vielleicht nie nach Schweden gekommen währe. Dank aan Lutgard en Peter voor hun steun gedurende de afgelopen drie jaar en hun gastvrijheid. Och på slutet: Tack till Klara - för kärleken och stödet under hela denna tid. Tack för att du finns.

Stephan Zimmer,
Stockholm & Brussels, September 2015

Part I

Galaxy Clusters and the Fermi Large Area Telescope

Chapter 1

Introduction

1.1 Introduction

Galaxy clusters are the largest structures in the Universe consisting of up to thousands of member galaxies that are bound by gravity. Initially they were considered to be distant extragalactic nebulae and their observations have provided important insights into the nature of our Universe. When F. Zwicky studied the motion of the galaxies in the Coma cluster he found that to explain the observed velocity dispersion of $1500 - 2000\,\mathrm{km\,s^{-1}}$ the average density in the Coma system would have to be at least 400 times larger than what can be inferred from luminous matter alone [174]. This observation led him to hypothesize that the cluster must be immersed in a halo of Dark Matter (DM).[1] Today observations from various astrophysical probes suggest that as much as 85% of the matter in the Universe is made up of DM which in fact provides the gravitational potential towards which smaller systems accrete to form clusters.

γ rays provide a unique astrophysical probe to study the most energetic phenomena occurring in the Universe and allow to study their origin as they travel in straight paths to the observer. Observations of the γ-ray sky have revealed that most of the emission we see originates from interactions of cosmic rays (CRs) in our own Galaxy. As clusters are conglomerates of galaxies, we can expect to see γ rays on the same grounds. In this thesis we use data taken by the Fermi Large Areal Telescope (LAT) to study the nearby most massive clusters and search for γ rays from them.

[1] Historically, the discovery of DM is attributed both to Zwicky based on his observations of the Coma cluster and was later confirmed by the observation of rotation curves of spiral galaxies by V. Rubin [145]. More recently it was found however, that the Swedish astronomer K. Lundmark was the first who hypothesized the existence of DM already three years before Zwicky [118].

1.2 Outline of the thesis

The outline of this thesis is as follows. Chapter 2 introduces the Fermi-LAT instrument to provide the experimental context for the work presented in this thesis. Chapters 3-5 are intended to help establishing the physical background by providing a description of the γ-ray sky and giving a brief introduction into the subject of clusters of galaxies, outlining some of the current open questions in regards to DM and CR physics in clusters. In chapter 6 we detail the more technical aspects of this work, discussing the employed data analysis methods used in this thesis. Lastly, in Chapter 7 we present the main findings of the accompanying papers, summarize our work and discuss its limitations. We close the chapter by providing a brief outlook as to the (detection) prospects with current and upcoming experiments. Some parts of the text in this thesis rely on work which I have documented in my licentiate thesis [172].[2]

1.3 The author's contribution

Paper I

The idea to use joint-likelihood in the context of CR-physics came from J. Conrad (as well as the idea to use it with Fermi-LAT data in the first place). He and myself led the project while I carried out the entire LAT analysis and wrote most parts of the initial manuscript, with the exception of the Introduction, §4.1 as well as the Discussion on Dutson et al. [87] which were written by my collaborators, C. Pfrommer and O. Reimer, respectively. All contact authors (J. Conrad, A. Pinzke, C. Pfrommer O. Reimer and I) worked together in discussing the applied methods, selection criteria and results as well as collaborated in revising the manuscript.

Paper II

I was responsible for the cluster-related aspects in this paper and shared the leadership together with my collaborator T. Jogler. To this end I carried out the LAT analysis pertaining the calculation of upper limits on the DM- and CR-induced γ-ray flux and wrote the relevant sections in addition to the introduction. J. Conrad provided numerous input during the analysis and helped overcome

[2] More specifically, the work presented in chapters 2.1-2.2, 3.2, 4.2.2, 5.1.1, the introduction to 5.2, as well as chapter 6.1 together with the summary of Paper I in chapter 7.1 are taken from my licentiate thesis with only minor modifications to the text.

the challenges we faced throughout the project. A. Pinzke contributed his expertise to the CR-modeling while T. Jeltema and E. Storm supplied the models for the leptonic annihilation channels in Virgo. Further contributions came from M. Gustafsson and M. Sánchez-Conde who provided the DM templates along with their boost-factor calculations.

Paper III

I shared the lead of the paper with my collaborators B. Anderson and J. Conrad. In this context, I wrote parts of the analysis framework and contributed with extensive simulations to the verification of the methods in addition to providing the spatial templates pertaining the DM profiles for each cluster. I also carried out some of the LAT-related analysis, even though the final limits were calculated by my collaborator, B. Anderson. He and I shared the responsibility for the draft, with the exception of the discussion which was mainly written by M. Gustafsson, and further input was made by the co-authors of the paper. All corresponding authors worked together in the discussion of the applied methods and results as well as on the revision of the manuscript.

Paper IV

I am the principle author who carried out the entire LAT analysis and wrote most of the manuscript. §2.1 and parts of the discussion were written by my collaborator Y. Rephaeli. The remaining contact authors (J. Conrad and O. Reimer) contributed to discussing the applied methods and conclusions of the paper. All contact authors contributed in the revision of the manuscript.

Other work not included in this thesis

As member of the *Fermi*-LAT collaboration, I have taken part in running large scale detector simulations which were then utilized, e.g. in the background estimation of Ackermann et al. [16] or in the creation of new IRFs [60] as well as for the development of Pass 8 [45] (see §2.3). For Pass 8 I further contributed to increasing the existing database of periodic triggers which are used to find better methods in the handling of instrumental pile-up (c.f. §2.2.3). In the MC context I contributed in optimizing the existing framework and planned, developed and comissioned an interface of the *Fermi*-LAT data processing pipeline to shared computing resources (GRID). This work was presented as poster contribution at CHEP 2012 and is documented in Paper VI. A number of technical reports discuss the current implementation and its performance for production-grade MC

simulations [43; 42; 113]. Initially for Paper I, but used throughout the analyses presented in this thesis, I developed a code to produce spatial emission templates to be used when performing data analysis of large extended sources.

1.4 Units, Conventions and Acronyms

This thesis, as far as the theoretical models are concerned adopts the Gaussian (CGS)-system of units where the base units are centimeter, gram and second. Below is a collection of units and conversions to particle physics units, often conveniently expressed in powers of electron-Volt (eV), the reader may find useful.

$$\begin{aligned} 1\,\mathrm{cm} &= 5.0677 \times 10^{13}\,\mathrm{GeV}^{-1} \\ &= 3.2408 \times 10^{-25}\,\mathrm{Mpc} \\ 1\,\mathrm{s} &= 1.5193 \times 10^{24}\,\mathrm{GeV}^{-1} \\ 1\,\mathrm{erg} &= 624.15\,\mathrm{GeV} \\ &= 10^{-7}\mathrm{J} \end{aligned}$$

We use $H_0 = 100h\,\mathrm{km\,s^{-1}\,Mpc^{-1}}$ for the Hubble constant, with $h = 0.7$ as the Hubble parameter [26]. The critical density of the Universe, ρ_c is then:

$$\begin{aligned} \rho_c = 3H_0^2/8\pi G &\simeq 1.9 \times 10^{-29} h^2\,\mathrm{g\,cm^{-3}} \\ &\simeq 10^{-6}\,\mathrm{GeV\,cm^{-3}} \\ &\simeq (5-6)\,\mathrm{protons\,m^{-3}}, \end{aligned}$$

with G being the gravitational constant $G = 6.6720 \times 10^{-8}\,\mathrm{cm^3\,g^{-1}\,s^{-1}}$. The most commonly used acronyms used in this thesis are listed in Table 1.1

Acronym	Meaning	Sections
ACD	Anti-Coincidence Detector	2.2, 2.3
AGN	Active Galactic Nuclei	3.2, 5.1
CAL	Calorimeter	2.2, 2.3
CC	Cool Core	4.2, 4.3,
CR	Cosmic Ray	2.3, 3.1-3.3, 4.2, 5.1
CRe	Cosmic Ray Electron	3.1, 4.3, 5.1
CRp	Cosmic Ray Proton	5.1, 7.1
CTA	Cherenkov Telescope Array	7.2
DM	Dark Matter	1.1, 4.1, 5.2, 7.1, 6.3
DSA	Diffusive Shock Acceleration	5.1, 7.1
EGB	Extragalactic Gamma Ray Background	3.3, 5.1
EGRET	Energetic Gamma Ray Experiment Telescope	2.1
FoV	Field of View	2.2
GTI	Good Time Interval	6.1
HIFLUCGS	HIghest X-ray FLUx Galaxy Cluster Sample	4.2, 6.5, 7.1
ICM	Intracluster Medium	4.1-4.3, 5.1, 7.1
IGRB	Isotropic Gamma Ray Background	3.3, 7.2
IRF	Instrument Response Function	2.3
LAT	Large Area Telescope	2
LOFAR	LOw Frequency ARray	4.3
MC	Monte Carlo	1.3, 2.2, 2.3, 6.2
MLE	Maximum Likelihood Estimate	6.2
NCC	Non Cool Core	4.2
NFW	Navarro-Frenk-White	5.2.2
PSF	Point Spread Function	2.2, 2.3, 6.5, 7.2
PWN	Pulsar Wind Nebula	3.2
ROI	Region of Interest	6.1, 6.3
ROSAT	Röntgen Satellite	4.2, 5.2
SN	Super Nova	3.2
SNR	Super Nova Remnant	3.2, 5.1
SSD	single-sided silicon strip detector	2.2
TKR	Tracker	2.2, 2.3
TS	Test Statistic	6.2, 6.5, 6.6
WIMP	Weakly Interacting Massive Particle	5.2, 7.1

Table 1.1. List of commonly used acronyms used in this thesis

Chapter 2

The Fermi Large Area Telescope

2.1 The Fermi satellite

The Fermi satellite was designed to succeed the EGRET instrument onboard the Compton Gamma Ray Observatory [160]. It was launched on June 11th, 2008 aboard a Delta II rocket and maintains a low-earth orbit at an altitude of about 550 km [48]. In nominal science operations, the satellite operates in survey mode and covers the entire sky every 3 hours (2 orbits). In order to achieve uniform exposure, the satellite performs a *rocking* motion perpendicular to the orbital motion. In the default profile, the satellite rocks between 50 degrees towards each direction during each consecutive orbit. In addition, the satellite may move from its survey mode into time-limited pointed observations (target-of-opportunity). During 2014, the LAT temporarily changed its orbit to a more biased one towards the galactic center (see, e.g. [122; 167]). This was in part to accumulate enough data to address recent claims of detection of DM [166; 154]. Since January 2015, the LAT has resumed its original orbit. Onboard the satellite are two scientific instruments, the gamma-ray burst monitor (GBM) (see, e.g. [54; 123]) and the LAT, which we discuss in detail in this chapter.

2.2 The Large Area Telescope

The LAT is the primary scientific instrument onboard the satellite. It is a pair conversion telescope and sensitive to γ rays above $\sim 20\,\mathrm{MeV}$ to a few TeV with a field of view (FoV) of 2.4 sr [48]. The low energy threshold is dictated by the fact that below $O(10)\,\mathrm{MeV}$, photons lose energy through Compton interactions

rather than producing electron-positron pairs. Consequently, the recorded tracks of these Compton events do not have vertices and the associated events are more difficult to reconstruct. On the high end, the size of the calorimeter with 8.6 radiation lengths limits the containment of the ensuing electromagnetic showers that develops when high energy particles interact in the calorimeter material, which in turn limits the event reconstruction at the highest energies.

2.2.1 Detector Components

The LAT employs an array of 4×4 tower modules [46]. Each module has 18 tracking planes and a calorimeter module. Figure 2.1 shows a schematic view of the LAT with its detector components and an overlaid γ-ray converting into an electron-positron pair. The key instrumental parameters of the LAT are summarized in table 2.1 [48].

The tracker (TKR) plane consists of 2 layers of single-sided silicon strip detectors (SSD), the first 16 of which are interleaved with tungsten to promote pair conversion while the last two layers are just comprised of single-sided SSDs. The tungsten layer also causes multiple scattering which worsens the angular resolution. To balance angular resolution and tracking abilities of the LAT, the tracker is divided into a front and back region. In the front (thin) section, each SSD plane is interleaved with a thin tungsten foil with 3% of a radiation length. In the back (thick) section these converter foils are about six times thicker [47].

The tower module behind the tracker is a segmented CsI(Ti) crystal calorimeter (CAL) [70]. When the electron-positron pairs interact with the calorimeter material, an electromagnetic shower develops and the deposited energy can be used to reconstruct the total energy of the incoming γ-ray.

Charged particle discrimination is achieved through a segmented anti-coincidence detector (ACD), consisting of plastic scintillator tiles acting as a charged particle "veto". Its design allows a charged particle rejection of over 99.97% and minimizes the detector deadtime due to backsplash considerably [125].

The principle trigger is issued when three adjacent x-y SSD planes in one tower report a signal above a predetermined threshold. In order to reduce the event rate to an acceptable level for data down-link but also to select events with energy deposits in the CAL above 20 GeV, an on-board filtering is performed. This limits the event readout of γ rays to about 350 Hz but also ensures that events with no associated TKR signature, so-called CalOnly events, are recorded [156].[1]

[1] Note that the trigger rate is about a factor ~ 10 higher. The rate of reconstructed γ rays that pass source class selection criteria on the other hand is about $O(1)$ Hz [17].

PARAMETER	VALUE OR RANGE
Energy Range	20MeV– 300GeV
Effective Area at normal incidence	$\sim 1\mathrm{m}^2$
Field of View (FoV)	$2.4\,\mathrm{sr}$
Event Readout time (dead time)	$26.5\,\mu\mathrm{s}$
Angular resolution (on-axis 68% containment radius) > 10 GeV	$\leq 0°.15$
On-axis, 95% containment radius	$< 3 \times \theta_{68\%}$
Off-axis, containment radius at 55°	$< 1.7\times$ on-axis value
Point Source Sensitivity (> 100 MeV)	$3 \times 10^{-9}\mathrm{ph\,cm^{-2}\,s^{-1}}$
Detector depth including tracker	10.1 radiation lengths
ACD segmentation into tiles	$< 1000\,\mathrm{cm}^2$ each (1 layer)

Table 2.1. Selection of key LAT parameters, compiled from tables 1-4 in Atwood et al. [48]. The large FoV allows the LAT to cover almost the entire sky after every two orbits. The segmented ACD tiles provide a substantially improved charge particle rejection with respect to the predecessor (EGRET) [160]. The point-source sensitivity has been evaluated for a steady source after one year of sky survey, assuming a high-latitude diffuse flux of $1.5 \times 10^{-}5\,\mathrm{cm^{-2}\,s^{-1}\,sr^{-1}}$ at $> 100\,\mathrm{MeV}$ and a single powerlaw with spectral index $\Gamma = -2.1$ [see 48, for details]

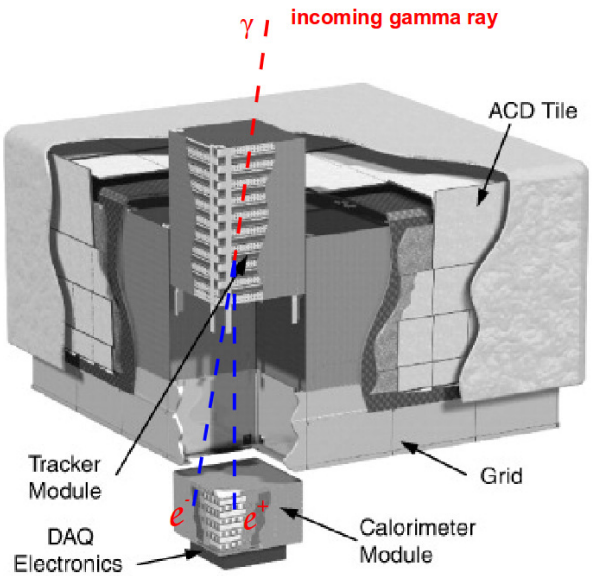

Figure 2.1. Schematic view of the LAT. The telescopes dimensions are $1.8\,\mathrm{m} \times 1.8\,\mathrm{m} \times 0.72\,\mathrm{m}$. Picture adapted from Atwood et al. [48].

2.2.2 Reconstruction Passes

The LAT-team updated its released data products (and reconstruction algorithms) to account for the improvement in instrument understanding. Each of these *passes* corresponds to a significant improvement and is summarized below:

1. *Pass 6*: performance entirely determined based on MC and pre-flight estimates
2. *Pass 7*: full on-orbit calibration of performance with minimal corrections from MC; P7REP refers to a re-processing of the data taken by the LAT with updated time-dependent calibration constants of parts of the detector [60].
3. *Pass 8*: consistent treatment of instrumental pile-up (see §2.3)

2.2.3 Instrumental Pile-up: Ghosts

Events entering the instrument during the finite dead time of the readout ($\sim 30\,\mu s$) caused remnant electronic signals. These pile-up events, or *ghosts*, have been determined to be the cause of early problems in the reconstruction algorithms and severely affect the performance of both the subsystems as well as the high level event analysis. Reducing the impact of instrumental pile-up has been at the core of Pass 8. In the Geant4-based detector simulation of the LAT [57; 117], ghosts are emulated by taking periodic triggers (at a frequency of 2 Hz) and *overlaying* these real events with the generated MC events. In Fig. 2.2 we show an example of a ghost event in the LAT.

2.3 Event Reconstruction, Classification and Analysis

Once the raw data is downlinked, an array of reconstruction algorithms is employed to convert the raw detector signal in high level information: tracks, calorimeter energies and ACD vetoes. In brief, the reconstruction can be separated into reconstructing the direction of the incoming γ ray and its deposited energy (For a detailed discussion see Section 2.4 in [48]). As mentioned in the previous section, the presence of ghosts has severely impacted the science potential of the LAT during its early mission. At the writing of this thesis the LAT is now in transition into Pass 8. Consequently, In this section I will give a brief account of the methods used prior to Pass 8 and those that will be used when this thesis is publicly defended.

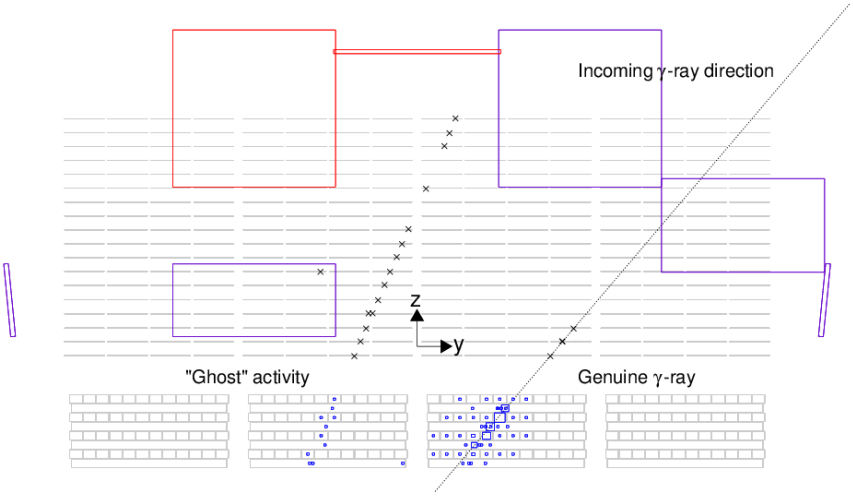

Figure 2.2. Example of a simulated ghost event in the LAT (y-z orthogonal projection), taken from Ackermann et al. [17]. In addition to the primary γ-ray signal that arises from a back-converting 8.5 GeV photon, the LAT experiences activity in all three subsystems: TKR, CAL and ACD. Each cross represents a hit in the tracker while the variable-sized squares indicate the location of the reconstructed energy deposit in each crystal in the CAL (larger energy release is associated with larger squares). The dashed line indicates the incoming γ-ray direction. For clarity, only ACD volumes with signals above the zero suppression level are shown.

Tracker

As discussed in the previous section, once multiple hits are detected in the tracker (three-in-a-row), an event is recorded. Based on the information from the tracker, a track hypothesis is constructed using a pattern-based approach (see Section 2.4.1 in [48]). After the track reconstruction, vertex solutions between two tracks are calculated retaining the full covariance matrix of each track. If additional calorimeter information is available, this may be used to improve the directional accuracy of the reconstructed tracks allowing a better determination of the direction of the incoming γ ray (Kalman filtering).

Changes with Pass 8: The pattern-based track reconstruction has been replaced by a *global* tree-based reconstruction method [45]. In this algorithm, hits in the tracker are linked together to one or multiple trees. The longest and straightest branch represent the primary electron-positron trajectories. Unlike the combinatorial pattern-based algorithm, this method does not rely on a track hypothesis and accounts for the fact that the event signature is not as simple as e.g. schematically shown in Fig. 2.1, with two clean trajectories arising from the electron-positron pair but rather resemble features of an extended electromagnetic shower. Also the tree-based pattern recognition approach does not need input from the calorimeter, as it was required for the pattern-based approach. If more than one track is found in a given tree, an attempt of determining its vertex is made. In the context of Pass 8, the vertexing scheme has been re-developed which takes multiple scattering better into account, leading to an overall improvement in the PSF.

Calorimeter

For the determination of the energy, two different algorithms are used: a parametric correction (PC) and a fit to the longitudinal and transverse shower profile (SP) [17]. The SP method only works beyond 1 GeV. The only method that provides an estimate over the entire energy range is the PC method. Classification trees are used to determine the best energy estimate for a given event along with a probability that the energy estimate is within the nominal core of the energy dispersion [17].

Changes with Pass 8: The most significant change that Pass 8 introduced at the CAL level is the concept of CAL clustering; instead of treating all calorimeter hits as a single monolithic entity, in P8, a clustering approach is taken instead. Similar to the new track-finding algorithm, all hits in the calorimeter are grouped together to form clusters using a minimum spanning tree algorithm (see, e.g. [121; 148]). Afterwards an energy-dependent threshold cut is applied

to 'prune' the tree. This allows us to effectively determine each sub-cluster in an event and helps to separate the primary γ-ray shower from the ghost-induced hits in the calorimeter. Aside from efficiently handling instrumental pile-up, the new CAL clustering enables us to reconstruct multi-γ-ray events, which could for instance be emitted from evaporating black holes (see, e.g. [161; 74]) In addition, the SP fit has been generalized into a full three-dimensional fit to the shower profile which allows to effectively reconstruct γ rays up to 3 TeV [63].

ACD

For the ACD reconstruction, the first step is to estimate the energy deposited in each tile and ribbon. In the next step, each previously found track is projected onto the ACD and an association is made. If there is no intersection of a track with a non-zero ACD element (tile or ribbon), the distance of closest approach is calculated instead. Afterwards, each ACD-TKR association is ranked according to the energy deposited in the ACD and the track distance from the ACD hit to determine the likelihood of the track being associated with a charged particle event. This information is used to determine whether or not to reject the event at a later stage.

Changes with Pass 8: The ACD reconstruction has undergone a major revision in the context of Pass 8. In addition to using the projected TKR tracks, the information from the CAL is used as well. Pass 8 also incorporates the event-by-event directional uncertainties during the association step. This allows a better characterization of the large topology of γ-ray events in addition to further improving the background rejection capabilities. Finally, Pass 8 includes the fast ACD signals to the LAT trigger, which assists in removing out-of-time signals from the ACD. This provides an increase in effective area, especially towards lower energies where CAL backsplash is minimal [45].

2.3.1 Event Level Analysis

During the reconstruction a number of *figure of merit* variables are calculated, i.e. those coming from the subsystems such as track variables, ACD tile hits or the reconstructed tracks and calorimeter clusters. Generally, these variables differ between γ rays and CR backgrounds. Classification trees are used to determine the best estimates for the event energy and direction as well as its likelihood of being a γ-ray. We trained our classification trees using simulated event samples. Event classes can then be defined through cuts in terms of γ-ray purity that range from *transient* (high statistics but potentially high CR contamination) to *ultraclean* (high purity but low statistics).

Changes with Pass 8: One main change introduced with Pass 8 is the use of boosted decision trees as part of the TMVA multivariate analysis framework [103]. Its use improves the background rejection capabilities equating to a larger γ-ray acceptance with respect to earlier passes (see next section for details). In Pass 7, events with CAL energy deposits < 5 MeV are discarded; Pass 8 utilizes the full detector information and introduces both CAL-only and TKR-only events, the latter associated with low ($\lesssim 100$ MeV) energy events.

2.3.2 Parametrising the detector response

The Instrument Response Functions (IRFs) are used to provide a parametrized form of the entire detector response. They are generated using full detector MC simulations of γ rays, calibrated in beam tests and utilized in science analysis.[2] In general, the response matrix R of any event that relates the true direction $\mathbf{x}$ and energy E with the measured direction $\mathbf{x}'$ and measured energy E' can be written as:

$$R(E', \mathbf{x}'; E, \mathbf{x}) = A(E, \mathbf{x}) \times D(E'; E, \mathbf{x}) \times P(\mathbf{x}'; E, \mathbf{x}) \tag{2.1}$$

where $A(E, \mathbf{x})$ refers to the effective area of the detector for detecting γ rays and $D(E'; E, \mathbf{x})$ and $P(\mathbf{x}'; E, \mathbf{x})$ denote the energy dispersion and PSF, respectively. The response of front and back-converting events is evaluated separately. Due to the changed acceptance for the different event classes discussed in the previous section, IRFs are evaluated separately for each of them.[3]

Effective Area

The LAT effective area is a measure of how efficiently γ rays can be detected with the LAT at a given energy. It is derived from full detector simulations of γ rays that take into account the physics interaction, event reconstruction, on-board filtering and digitization and also the event analysis (background rejection) For a detailed discussion the reader is referred to Section 3.3 in Ackermann et al. [17].

[2] The term full detector simulation refers to the Geant4-based simulation of the LAT, *gleam* [57], while the fast simulation package *gtobssim* employs the IRFs instead.

[3] Pass 8 extends this concept by introducing IRFs for quantiles of energy-dispersion and PSF. Both the parametrization of the PSF and the energy dispersion have been updated to reflect our improved understanding of the LAT [T. Desgardin, private communication].

Point Spread Function

The LAT uses a double King-profile [108; 141] to parametrise its PSF in terms of the scaled angular deviation, x:

$$x = \frac{\delta v}{S_P(E)}, \tag{2.2}$$

where the energy dependence of the PSF is contained in the scaling term $S_P(E)$ and the deviation between measured and true position is denoted as δv. The scaled deviation, split into a core and a tail part of its pdf, can then be written as:

$$P(x) = f_{\mathrm{core}} K(x, \sigma_{\mathrm{core}}, \gamma_{\mathrm{core}}) + (1 - f_{\mathrm{core}}) \times K(x, \sigma_{\mathrm{tail}}, \gamma_{\mathrm{tail}}) \tag{2.3}$$

where $K(x, \sigma, \gamma)$ is the aforementioned King-function with the shape parameters σ and γ, computed separately for the core and the tail of the distribution:

$$K(x, \sigma, \gamma) = \frac{1}{2\pi\sigma^2}\left(1 - \frac{1}{\gamma}\right) \times \left[1 + \frac{1}{2\gamma} \times \frac{x^2}{\sigma^2}\right]^{-\gamma}. \tag{2.4}$$

The values for the shape parameters ($\sigma_{\mathrm{core}}, \gamma_{\mathrm{core}}, \sigma_{\mathrm{tail}}$, and γ_{tail}) and the scaling of the core part, f_{core} are contained in the FITS files that are used in the analysis of LAT data.

One can quantify the PSF by the containment radius of the distribution of the incoming γ rays, which is usually expressed in degrees. The PSF varies inversely with energy and is $\sim 10^\circ$ at $100\ \mathrm{MeV}$. This inverse relationship is due to multiple scattering which makes the track reconstruction difficult at these energies. A useful approximation for the 68% containment radius (in degrees) for front-converting events is [19]:

$$\theta_{68}(E) = \sqrt{((3.5/E)^{-0.8})^2 + 0.15^2} \tag{2.5}$$

Back-converting events have a PSF that is about twice that size.

Energy Dispersion

The energy dispersion plays a crucial role when searching for spectral features, such as monochromatic γ-ray lines as would be expected from DM scenarios or breaks in the spectrum, such as the one studied in Paper IV. The energy dispersion is mainly limited by the finite size of the calorimeter coupled with

the methods used to determine the energy (see previous section). Similar to the PSF, we introduce the scaled deviation x,

$$x = \frac{E' - E}{S_D(E,\theta) \times E} \tag{2.6}$$

where S_D is an empirically determined energy and angle-dependent scaling term:

$$\begin{aligned} S_D(E,\theta) &= c_0(\log E)^2 + c_1 \cos^2\theta + c_2 \log(E) \\ &\quad + c_3 \times \cos\theta + c_4 \times \log E \times \cos\theta + c_5 \end{aligned} \tag{2.7}$$

where c_i are pre-tabulated values. We use a Gaussian-like function to parametrize the energy dispersion, introducing the Rando-function, R [17]:

$$R(x, x_0, \sigma, \gamma) = \exp\left(-\frac{1}{2}\left|\frac{x - x_0}{\sigma}\right|^{\gamma}\right). \tag{2.8}$$

Finally, we can express the energy dispersion D as piece-wise Rando-function:

$$D(x) = \begin{cases} N_L R(x, x_0, \sigma_L, \gamma_L) & \text{if } (x - x_0) < -\tilde{x} \\ N_l R(x, x_0, \sigma_l, \gamma_l) & \text{if } (x - x_0) \in [-\tilde{x}, 0] \\ N_r R(x, x_0, \sigma_r, \gamma_r) & \text{if } (x - x_0) \in [0, \tilde{x}] \\ N_R R(x, x_0, \sigma_R, \gamma_R) & \text{if } (x - x_0) > \tilde{x} \end{cases} \tag{2.9}$$

$$\tag{2.10}$$

In Figs. 2.3 and 2.4 we show a panel of the effective area, the energy dispersion and the PSF at normal incidence as function of energy for the IRF versions used in this thesis.[4]

Propagating Systematic Uncertainties: bracketing IRFs

In order to propagate the uncertainties on the different IRF components, this thesis uses a bracketing approach, as discussed in §5.7.1 and §6.5.1 of Ackermann et al. [17]. In brief, we can construct a scaling function $B(E)$ which is used to determine the bracketing scale. The simplest choice, which maximizes and minimizes the systematic uncertainty in either effective area or PSF, respectively is

[4] For the latter we consider the 68% containment for simplicity and illustration purposes.

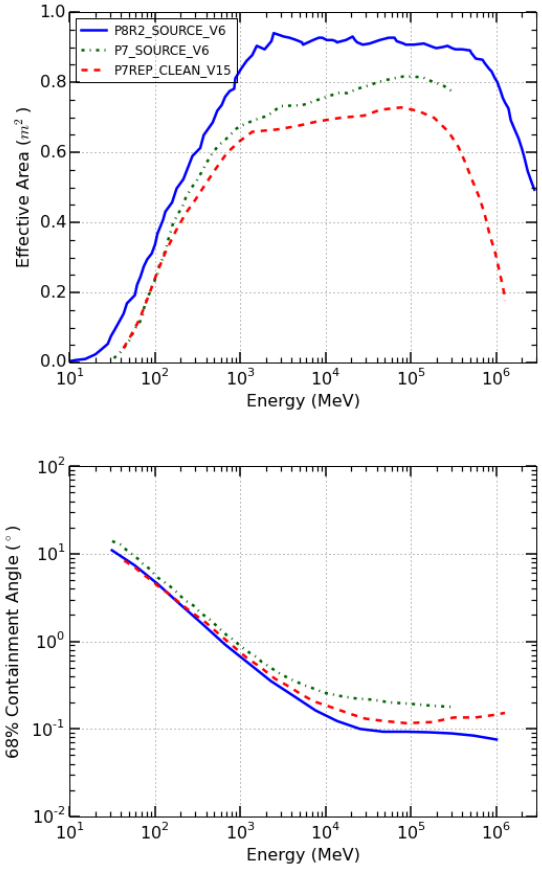

Figure 2.3. Performance plots for P7REP_CLEAN_V15 (Paper I and Paper III, red, dashed line), P7_SOURCE_V6 (Paper II, green, dash-dotted line), and P8R2_SOURCE_V6 (Paper IV, blue, solid line). The *top* panel shows the effective area and the *bottom* panel the PSF (or rather the 68% containment radius) for photons at normal incidence as function of energy that have been summed for front and back converting events. Note that the γ-ray-purity of SOURCE events in P8R2 corresponds to CLEAN events in P7REP.

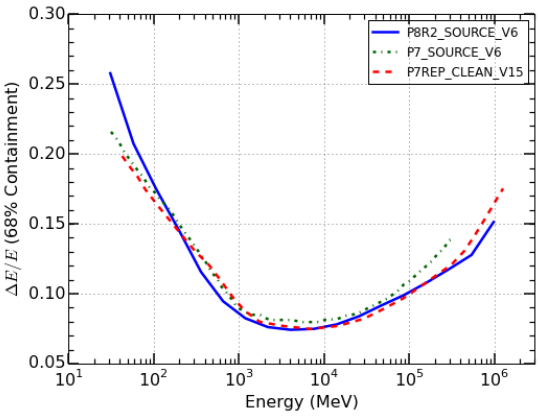

Figure 2.4. IRF Performance: energy dispersion. Line styles same as in Fig. 2.3.

$B(E) = \pm 1$. Paper I only considers the bracketing of the effective area term in the IRF. The modified effective area $A'(E, \mathbf{x})$ is given by:

$$A'(E, \mathbf{x}) = A(E, \mathbf{x}) \times (1 + \epsilon(E)B(E)) \tag{2.11}$$

For the values of $\epsilon(E)$, the values in Ackermann et al. [17] are used. Paper II and III extend this and also scales the PSF, where for simplicity we scale $\gamma_{\rm core}$. We can then express the modified PSF in terms of 68% containment radius, R_{68} and $r = R_{95}/R_{68}$:

$$\begin{array}{rcl} R'_{68} & = & R_{68}(1 + \epsilon_{68}B_{68}(E)) \\ r' & = & r(1 + \epsilon_r(E)B_r(E)) \end{array} \tag{2.12}$$

with the same bracketing function $B_r(E) = B_{68}(E) = B(E) = \pm 1$ to represent the maximum and minimum values, respectively. Specifically, for Paper II and III we define the max IRF as the combination of A and P that maximize the effective area and give the best PSF while the min IRF is the combination that minimizes A and maximizes P. In table 2.2 we summarize the datasets, IRFs and which IRF uncertainties are included in the accompanying papers.

PAPER	DATASET (EVENT CLASS)	IRFS	ENERGY DISP.	IRF UNC.
I	P7REP (Clean events)	P7REP_CLEAN_V15	No	effective area
II	P7 (Source events)	P7_SOURCE_V6	No	None
III	P7REP (Clean events)	P7REP_CLEAN_V15	Yes	effective area, PSF
IV	P8R2 (Source)	P8R2_SOURCE_V6	Yes	effective area, PSF

Table 2.2. Summary of datasets, IRFs and which IRF uncertainties have been assessed in the accompanying papers to this thesis. The energy dispersion column indicates whether the energy dispersion has been accounted for in the likelihood analysis.

Chapter 3

The γ-ray Sky

When viewing the γ-ray-sky, we are observing photons that arise from phenomena that involve extreme energies and environments. For instance, strong magnetic fields or remnants of supernova explosions provide the environment that is required to accelerate CRs to relativistic energies. In this chapter we give a brief run-down of known γ-ray-emitters.

3.1 Galactic Diffuse emission

Above 50 MeV the dominant γ-ray emission the LAT sees originates from within our own Milky Way and its flux is about five times that of all resolved sources observed by the LAT.[1] CR nucleons, subjected to inter-galactic magnetic fields, interact with one another and with the radiation fields in the Galaxy. Leptonic and hadronic interactions give rise to different γ-ray signatures along with contributions from Bremsstrahlung and inverse Compton (IC) emission that primarily arises from CR electrons (CRe) interacting with the Galactic radiation fields (starlight, emission from dust particles and the cosmic microwave background, CMB). The resulting spectrum is then a complex superposition of these individual contributors and subject to many uncertainties, such as the magnetic field configurations, sites of CR production and identifying the transport mechanism that causes CRs produced in Galactic sources to diffuse out towards the edge of our own Galaxy.

Part of this complexity can be seen when looking at a projection of the γ-ray sky as shown in Fig. 3.1. The projection is chosen such that the emission from the Milkyway is concentrated along the bright horizontal band (which we

[1] At lower energies, the dominant γ-ray source is the so-called Limb of the Earth. Here CRs interact with the nucleons in the atmosphere and produce γ rays [23].

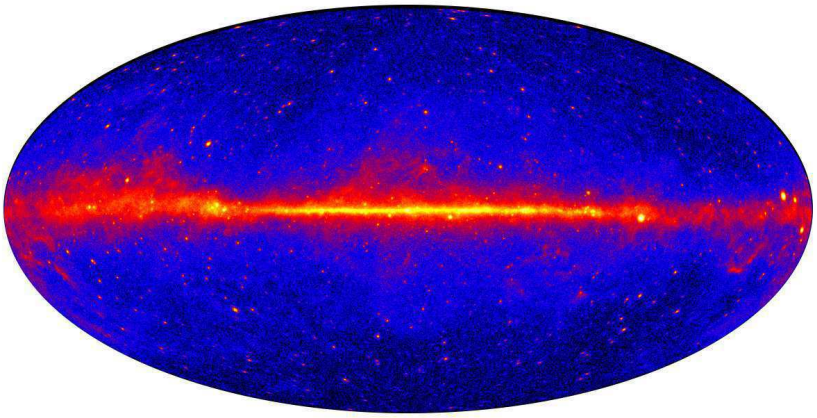

Figure 3.1. Hammer-Aitoff projection of the sky as seen in γ rays. The map is based on 5 years of integrated *Fermi*-LAT exposure above 1 GeV [credit: NASA/DOE/*Fermi*-LAT Collaboration]. Brighter colors correspond to brighter γ-ray sources. For visualization purposes the map has been adaptively smoothed with a energy-dependent kernel.

refer to as Galactic plane). A second look (in particular off-plane) at the same figure also hints at the existence of large scale structures, one of them being the Fermi "bubbles" [155; 12], a pair of two lobes extending up to $\pm \sim 50^\circ$ in Galactic latitude (or about 25000 light years) and about 40° in longitude whose astrophysical origin is unclear to date (see, e.g. [12; 79] for a recent discussion). One key aspect in understanding how γ rays can be observed from these structures concerns the target material (the interstellar gas) and the γ-ray emissivity of the different involved gas molecules. The majority of the interstellar gas is comprised of atomic and molecular hydrogen. While the former can be traced directly using the 21 cm hyperfine line, the latter can only be traced indirectly, for instance using the CO line at 2.6 mm. Lastly ionized hydrogen gas (H_{II}) is traced in multiple ways, for instance via the 656 nm H_α transition line.

3.1.1 Standard Diffuse Model

Identifying fainter sources that are buried underneath the foreground emission, we require a detailed model [71]. Using the various tracers, a composite model was created to model the contribution from the interstellar gas. The model is complemented with empirical templates to Galactic structures such as the Fermi bubbles and local supernova remnant shells, the most prominent being Loop I [72]. Another component concerns the contribution from IC emission. Here a

model with a radially symmetric distribution of pulsars as CR source is included and the numerical code GalProp [164] is used to calculate the resulting γ-ray-flux. After removing identified LAT sources (c.f. §3.2), this multi-component model is fit to LAT data in a global (i.e. all-sky) maximum likelihood fit to determine the relative contribution from each of the aforementioned components.

Caveats & Alternative Models

This template fitting creates residual structures, which however, are not clearly associated with individual sources. For the current diffuse model, these structures (above a certain scale size) are then re-injected and a fit is performed to obtain an improved model [71]. This procedure is motivated by the fact that the diffuse model is specifically designed to aid the searches for new point sources that become part of a catalog. However, in searches for faint extended emission, as the one studied in this thesis, the procedure to obtain the standard model poses a challenge due to the inclusion of the aforementioned residual structures. In addition, the determination of the IC contribution is highly dependent on a large number of diffusion parameters, such as the underlying source distribution, the height of the Galactic halo, magnetic fields, etc. These parameters are however poorly constrained and remain a topic of current research (see, e.g. [81] for a review).

The accompanying papers address this challenge in two different ways: a) avoiding the possible contribution from residual structures (Paper I) and b) attempt to quantify the effect of the diffuse emission modeling (Paper II and Paper IV).[2] We assess the uncertainty in the diffuse emission by repeating our analyses with a set of eight alternative diffuse models. These models differ from the standard template model in that they explore some of the parameter range of propagation parameters such as halo height (4 and 10 kpc), source population (supernova remnants or pulsars) and spin temperature (100K or optically thick), which were found to be most important when studying the diffuse γ-ray emission along the plane (where this emission is strongest) [11]. Note that these models were specifically selected for assessing the uncertainty when studying Galactic Supernova remnants (SNRs) which are extended in nature, but located along the Galactic plane [80]. To date, studying a specific region of interest and explore its dependence to different foreground model parameters such as the ones discussed here is the only way to obtain a qualitative estimate of the uncertainties associated with the Galactic diffuse emission.

[2] Paper III focuses on high energy ($E > 10\,\mathrm{GeV}$) photons and the diffuse background is determined locally from a maximum-likelihood fit, thus eliminating the need for a dedicated diffuse model.

3.2 A census of discrete γ-ray emitters: source catalogs with *Fermi*-LAT

Providing ever deeper catalogs of γ-ray emitters seen by the LAT remains a core responsibility of the *Fermi*-LAT collaboration. To date, three iterations have been released, spanning the MeV-GeV emission range (1FGL–3FGL) along with some dedicated catalogs focusing on high energy emission (1FHL [21] and 2FHL [35]). In the following section we briefly review the various γ-ray source classes:

- *Super Nova Remnants*: When a supernova (SN) explodes, massive amounts of energy are released. SNRs are formed from the outer layers of a pre-SN star as they are typically being ejected in shells. In these shells, particles are accelerated via Fermi-acceleration [165]. Recent studies revealed that they can even accelerate hadrons that give rise to π^0-production which decay to γ rays observable by *Fermi*-LAT. The hadronic origin can be proved by detecting the characteristic π^0 decay cut-off [18]. The LAT-detected SNRs are of Galactic origin.

- *Pulsar Wind Nebulae (PWN)*: These are nebulae that are powered by the magnetized particle wind stemming from pulsar emission. They can be found inside the shells of SNRs and allow acceleration of particles to energies at which γ rays are produced eventhough the SNRs have lost this ability (see, e.g. [116]). A classic example of a PWN is the Crab nebula, seen in γ rays both by the LAT and by ground-based air Cherenkov-telescopes such as H.E.S.S. or Veritas [33]. In the past the Crab has been used as standard candle due to its stable emission characteristics. This has changed recently with the detection of flaring γ rays being emitted by the pulsar inside the nebula (see, e.g. [40] for detection of the Crab pulsar at $E \gtrsim 100\,\mathrm{GeV}$ by Veritas). Together with SNR and AGN, PWN have been shown to accelerate particles giving rise to GeV-TeV-γ rays (see, e.g. [31]).

- *Pulsars*: These objects are fast rotating neutron stars left behind from explosions of massive stars from the main sequence with masses of $\sim 10\,M_\odot$. Powered by the fast rotation, they emit radiation from the radio to the γ-ray band. One particular class of pulsars are millisecond pulsars (MSPs), which spin much faster than ordinary ones [1]. Today about ~ 100 MSPs have been found, indicating large populations of MSPs in our own galaxy (see, e.g. [88]). There exists observational evidence of X-ray nebulae surrounding MSPs, indicating a population of relativistic

electrons and positrons [151; 107]. By this token, the increasing number of MSPs, may be able to account for the observed electron-positron asymmetry detected by Pamela [28; 29] and confirmed both by *Fermi*-LAT and the AMS experiment onboard the International Space Station at high energies [16; 30].

- *Starburst Galaxies*: Starburst galaxies are systems with very high star formation rates (between 0.1 and 10 $\mathrm{M}_{\odot}\,\mathrm{yr}^{-1}\,\mathrm{kpc}^{-3}$), [115]. Starburst activity is thought to be triggered by the close encounter or collision with another galaxy, producing regions of high gas densities and increased SN explosion rates, leading to a sizable number of SNRs. To date, only four nearby ($z < 0.005$) starburst galaxies have been found to be associated with GeV γ-ray-emission [15; 100]. However, given the observed tight correlation between γ-ray and infrared luminosity of these objects, it is conceivable that with more exposure the LAT could detect additional starburst galaxies over the course of its mission [15].

- *Active Galactic Nuclei (AGNs)*: AGN constitute the largest population of LAT sources, contributing to more than 90% of all LAT-associated sources (based on the latest catalog [10], hereafter referred to as 3FGL). Typically they are classified based on their emission characteristics (such as whether or not they are detected in various bands) and their orientation with respect to the observer (Seyfert galaxies, blazars, quasars and radio-galaxies). AGNs host a supermassive black hole and an accretion disk in the nucleus of an active galaxy. They provide efficient accelerations of CR to relativistic energies, emitting particles in collimated beams giving rise to γ rays in the GeV or even TeV regime (see, e.g. [116] and references therein). AGN play an important role in the physics of Galaxy clusters as they constitute the engines through which energetic particles are continuously injected into the cluster throughout its lifetime.

- *Other sources*: Other sources seen by the LAT include novae (bright explosions of the surface material in white dwarfs acquiring mass from massive companion stars), globular clusters or nearby (radio) galaxies such as the Large or Small Magellanic Cloud [8; 4], the latter which, similar to PWN and SNRs are extended γ-ray emitters.

Out of the roughly $\sim$ 3000 3FGL sources, 25 are modeled as spatially extended sources [114]. These are mainly Galactic SNR and PWNs as well as some nearby (radio) galaxies, such as Centaurus-A (or rather its extended lobe emission in γ rays [5]) as well as the Magellanic clouds [8; 4]. While many

of the LAT sources have been observed in other wavebands, a non-negligible fraction of the LAT sources lacks clear counterparts [6; 130; 10]. Fig. 3.2 shows the full sky map of 3FGL sources and their classification. In 1FGL, the first *Fermi*-LAT catalog, most sources are described by featureless single power-law spectra but throughout the development of later catalogs (2FGL and 3FGL, respectively) these models have become more sophisticated, accounting for curved spectra and spectral breaks [130; 10].

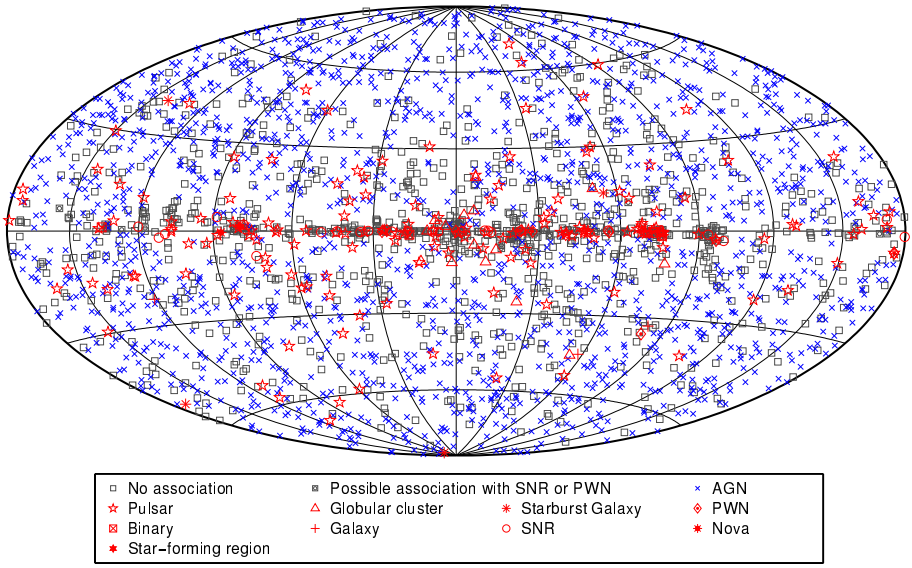

Figure 3.2. *Top:* sky map (Hammer-Aitoff projection), from Acero et al. [10]. Note that for clarity, all AGN classes are plotted with the same symbol.

3.3 Everything else: the Isotropic Gamma Ray Background

If both the Galactic foreground emission and the previously discussed discrete sources are removed from what is observed, we find that there is a non-negligible third contribution.[3] It is approximately spatially isotropic and at energies $\gtrsim$

[3] In fact, the existence of an isotropic γ-ray background has been seen already with OSO-3 [77; 110] and was later confirmed by measurements using the SAS-2 satellite [90; 91]

1 GeV, its intensity is comparable to that of the Galactic foreground emission. We refer to this as isotropic (or sometimes extragalactic) γ-ray background (IGRB) emission. Its emission has been measured from 100 MeV up to 820 GeV and it can be separated into true γ-ray emitters and the contamination from CR interactions which are misclassified as γ rays in the detector (c.f. §2.3). A related quantity is the extragalactic γ-ray background (EGB), a superposition of γ-ray emission observed from sources at the edge of the Milky Way to the edge of the observable Universe. These sources, similar to what *Fermi*-LAT already sees, include unresolved populations of AGNs, star-forming galaxies and γ-ray bursts in addition to LAT-detected extragalactic sources ($|b| > 20^\circ$). Over the energy range of 100 MeV– 100 GeV, the IGRB spectrum can be well fit with a featureless power-law with index ~ 2.3, at ~ 250 GeV, a spectral break occurs, which can be fitted with an exponential decay, shown in Fig. 3.3 [24]. Recent works suggest that as much as $\sim 50\%$ of the deduced EGB flux can be attributed to the emission coming from blazars [36].

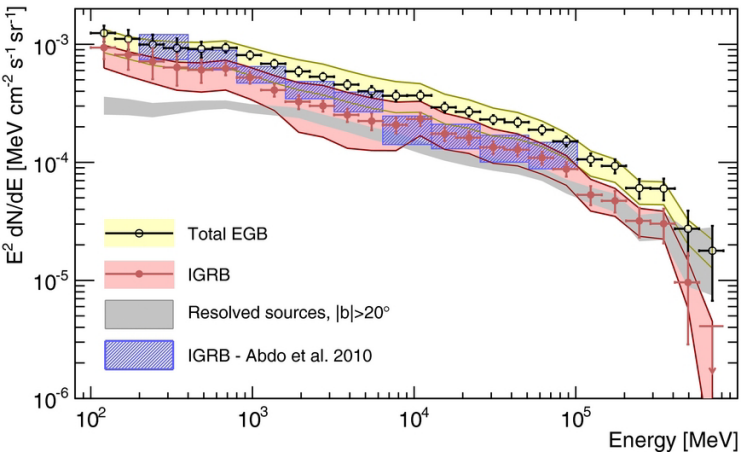

Figure 3.3. Measured spectrum of the isotropic γ-ray background, taken from Ackermann et al. [24]. The total EGB intensity is the sum of the IGRB and the intensity of resolved LAT sources at high Galactic latitudes $|b| > 20^\circ$. The shaded bands represent the uncertainties associated with the Galactic diffuse foreground modeling and the error bars on the measurement correspond to statistical and systematic uncertainties (from CR contamination), added in quadrature. The blue shaded band shows the first measurement of the IGRB with *Fermi*-LAT [9].

Chapter 4

Clusters of Galaxies

In this chapter we introduce galaxy clusters and discuss briefly how they formed and what can be learned from X-ray and radio-observations. Note that we leave the discussion on the origin of the observed radio emission for the subsequent chapter.

4.1 Formation and Evolution of Clusters

In our current model of a hot big bang, the Universe has three components, matter, radiation and a third one, often referred to as cosmological constant, denoted Λ. While radiation dominated the Universe during early times (up to redshifts, z, ~ 1000), matter took over and dominated the evolution of the Universe up to $z = 0.5$ at which Λ started to dominate. Matter here is referred to as luminous (baryonic, ordinary) matter and invisible (non-baryonic) cold DM. The latest measurements by the Planck satellite [27] indicate that the Universe consists only of only 4% of ordinary matter while the majority is either DM (27%) or dark energy (the remaining 69%), which may be identified as non-zero cosmological constant (see, e.g. [52] for a discussion of the role of Λ).

The formation of structures is believed to be driven by the gravitational collapse of the initial density fluctuations in an expanding Universe. As the Universe expands, these structures lose contact with one another and as consequence freeze in. The gravitational potential towards these over-densities causes both baryons and DM to accrete towards it. Structures than form (hierarchically) through a sequence of mergers and accretion of smaller systems. Clusters are the largest and latest to form and may even be virialized, i.e. gravitationally

stable. With $W_{\rm vir}$ being the potential energy of the cluster and $K_{\rm vir}$ being the kinetic energy associated with mergers, virialization is attained if:

$$-W_{\rm vir} = 2 \times K_{\rm vir}. \tag{4.1}$$

The virial theorem along with measurements of the velocity dispersion σ_v can be used to obtain a crude estimate of the total projected mass of the system at a distance D_A. Together with photometric observations the total light can be measured, providing an estimate to the total mass-to-light ratio, which for clusters is $M/L \sim O(300)$ [118; 174].

4.1.1 Structure and Content

While the vast majority ($\sim 85\%$) of the mass in a cluster apparently is in form of dissipation-less cold DM, the bulk of the baryons is present as gas, the intracluster medium (ICM) [124]. The infalling gas is heated to high temperatures ($\sim 10^6 K$) by strong accretion shocks associated with cluster mergers. At these temperatures, the gas emits (thermal) X-rays, eventually settling in a hydrostatic equilibrium within the gravitational well of the cluster.[1] Finally, as the gas density increases, it can both fuel star formation and accretion onto the super massive black holes present in the largest cluster member galaxies, both processes that cool the plasma. This cooling process can then result in an energetic feedback due to SNes or AGNs which in turn can inject substantial heat into the ICM leading to a cyclic process.

4.2 Observations with X-Ray telescopes

Observations of the ICM with X-ray telescopes have been key to understanding cluster physics such as the aforementioned cooling, shock heating but also when studying the chemical composition of the ICM. The spatial templates we use to model the CR-induced γ-ray emission from the clusters (refer to the next chapter for details) we studied in this thesis (Paper I, Paper II) were developed based on these measurements, such as the temperature profile of the ICM along with its morphology. Initially, X-ray observations were primarily limited to the cluster core $r \lesssim R_{2500}$, but more recently, several clusters were studied out to the virial radius.[2] The virial radius is taken to be the radius within which the mean

[1] Note that the assumption of hydrostatic equilibrium is a simplifying one that does not take into account the details of ICM physics and the X-ray gas is never fully thermalized. This can lead to a systematic bias in the mass estimate of 5-20% (see, e.g. [111; 126; 133]).

[2] R_{2500} is defined as the radius within which the mean matter density is $2500 \times \rho_c$.

matter density is $\Delta_{\rm vir}\rho_c$, with ρ_c being the critical density of the Universe. We commonly take $\Delta_{\rm vir} = 200$ and consequently find the virial mass, M_{200} defined as:

$$M_{200} = \frac{4\pi}{3} \times \rho_c \times 200 \times r_{200}^3, \tag{4.2}$$

with r_{200} being the virial radius.[3]

4.2.1 Galaxy Cluster Selection

All sample studies covered in this thesis (Paper I and Paper III) rely on a selection which is based on the HIghest X-ray FLUx Galaxy Cluster Sample (HIFLUCGS) cluster catalog, which provides a complete flux-limited sample of rich nearby ($z \lesssim 0.2$) X-ray luminous clusters $f_X(0.1 - 2.4\,\mathrm{keV}) \gtrsim 2 \times 10^{11}\,\mathrm{ergs\,s^{-1}\,cm^{-2}}$ with varying morphology [142; 75]. HIFLUCGS is a composite catalog based on inputs from a number of X-ray flux limited surveys (mostly based on ROSAT) (see [142] for further details). Using pointed ROSATs Germanium Position Sensitive Proportional Counters observations [89] and gas temperatures from ASCA [157], gravitational masses were computed assuming hydrostatic equilibrium. Among the important findings reported in Reiprich & Böhringer [142] is a strong correlation between X-ray luminosity and gravitational mass [142] with respect to the sample of 63 HIFLUCGS clusters.[4] In Fig. 4.1 we show a projection of the γ-ray sky and overlay the central coordinates of the clusters studied in this thesis.

4.2.2 Morphological Classification

While most clusters were initially detected in optical wavebands, X-ray observations such as the ones conducted with ROSAT and later Chandra and XMM-Newton revealed that there exist two fundamentally different classes of clusters. Cool core clusters (CC) contain very dense gaseous core regions while Non Cool Core (NCC) clusters show shallower cores along with structures indicating past or ongoing merger activity (see, e.g. [75] and references therein). In Paper I we follow the methodology put forward by Hudson et al. [104] considering 17

[3] Note the related radius R_{500} being defined as the radius in which the over density equals 500 times the critical density.

[4] Note that the original HIFLUCGS catalog considers 63 brightest clusters with $|b| \gtrsim 20^\circ$, the papers associated with this thesis refer to the extended HIFLUCGS catalog instead, containing 106 objects in total (including the Virgo cluster), including some that are located more closely towards the Galactic plane. The additional 43 clusters not included in the original catalog do not follow the originally imposed rather strict selection criteria [142].

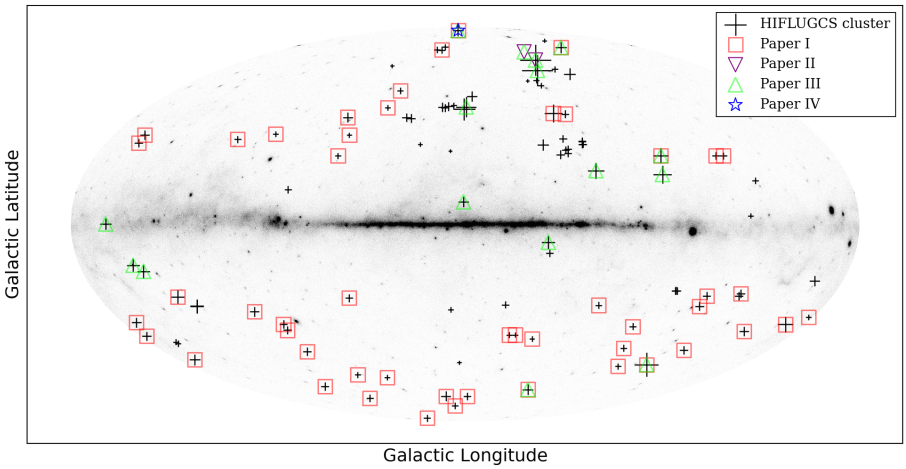

Figure 4.1. Hammer-Aitoff projection of Fermi-LAT counts map above 1GeV for 5 years of LAT exposure. Black crosses represent the projected direction of the 106 clusters in the extended HIFLUCGS catalog with the cross size corresponding to the distance to the cluster (larger crosses being more nearby systems). Colored markers represent the sub samples studied in the accompanying papers of this thesis.

different characteristics (e.g. central entropy, central surface X-ray brightness, central electron density etc.) to separate the clusters we study into CC and NCC, respectively.

4.3 Non-thermal Emission: Diffuse Radio Emission

Observations of Galaxy clusters with radio telescopes have revealed two kinds of structures: radio halos and relics which due to their observed synchrotron emission are indicative of a population of relativistic CRes within the ICM. Halos appear in two forms, giant (Mpc-sized) unpolarized diffuse structures which show a spatial distribution similar to that of the ICM, and mini halos, small ($\lesssim 500$ kpc) structures that surround powerful radio galaxies (e.g. the mini halo around NGC 1275 in the Perseus cluster [149]).[5] Mini halos are typically found at the centers of CC clusters while giant halos are often detected in the largest

[5]Note in comparison that the diameter of the Milky Way is less than 10% of the size of typical mini halos [170].

merging systems (such as the radio halo in Coma, [159; 62]). Brunetti et al. [65] found a strong correlation between the radio flux at 1.4 GHz and the X-ray luminosity of clusters with radio halos, further supporting the use of X-ray observables to help define a suitable sample of clusters.

Lastly, relics are linearly polarized peripheral structures with irregular morphology. In some cases, a spatial correlation with shocks in the thermal gas has been found [37]. A few examples of these radio structures are shown in Fig. 4.2. However, of all X-ray-observed clusters to-date, only a fraction show signs of non-thermal diffuse components, although with the advent of high-sensitivity low-frequency radio telescopes such as the low frequency array (LOFAR), this number is expected to grow [73].

4.3.1 Magnetic Fields

Measurements of the spectrum of these radio structures indicate a power-law behavior with a rather steep spectral index ($\alpha \gtrsim 1$) which provides evidence for a synchrotron origin necessarily along with weak magnetic fields. Currently, the best direct measurements of the magnetic field in the ICM come from Faraday-Rotation measurements (FRM) of radio sources in the field of the Coma cluster [58]. These observations indicate a central magnetic field of $\sim 3.9 - 5.4\,\mu G$. The detailed mapping of the FRM indicates that the magnetic field exhibits signs of Kolmogorov-type turbulence on all scales [109], even though the exact morphology of the magnetic field in clusters remains uncertain. Indirectly, magnetic fields can be inferred from the observed radio emission as discussed in the previous paragraph (given assumptions on the parent electron populations). The observation of synchrotron emission is however not sufficient to disentangle the underlying CRe distribution from the magnetic fields as these are degenerate. Hard X-rays originating from IC with the CRes or γ rays from the ICM however constitute useful signatures to break this degeneracy [64].

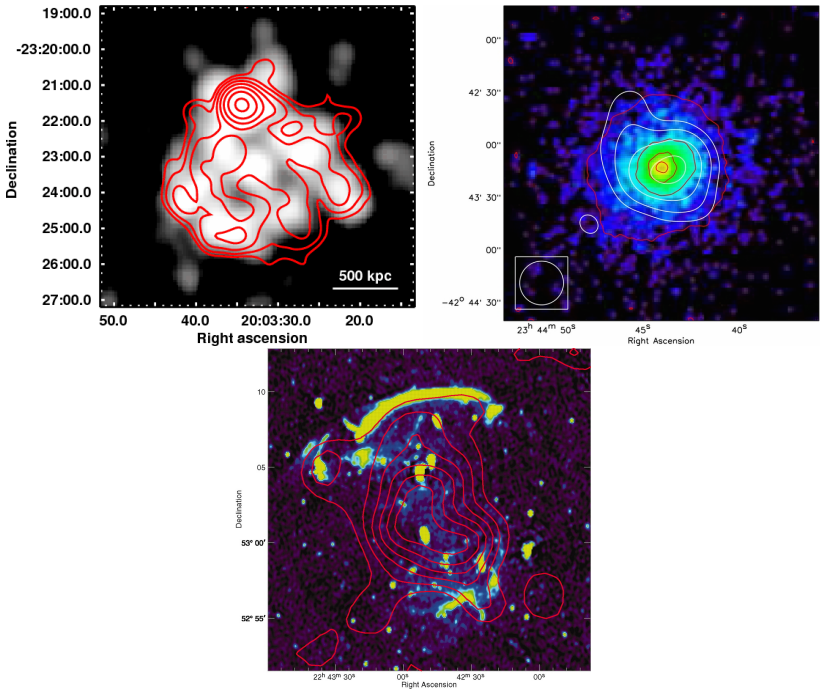

Figure 4.2. Compilation of Radio halos and relics. *Top Left:* VLA 1.4 GHz contours (red) of the giant radio halo in RXC J2003.5-2323 (z=0.317), superimposed on 610 MHz image from the Giant Metrewave Telescope, GMRT (grey scale) The 1σ level is $30\,\mathrm{mJy\,beam^{-1}}$ at 1.4 GHz and $100\,\mathrm{mJy\,beam^{-1}}$ at 610 MHz. Contours are spaced by a factor 2, starting from $\pm 0.09\,\mathrm{mJy\,beam^{-1}}$ (Image credit: [96]). *Top Right:* Chandra X-ray image $(0.5 - 2.0\,\mathrm{keV})$ of the Phoenix cluster at $z = 0.596$ overlaid with GMRT radio contours at 610 MHz. The circular beam size is 25" and indicated in the inset (Image credit: [163]) *Bottom*: 1.4 GHz observations with the Westerbork Synthesis Radio Telescope of CIZA J2242.8+5301 (z=0.1921) with overlaid X-ray contours from ROSAT. The radio map features an elongated relic towards the North of the cluster, giving it the nickname "sausage" (Image credit [162]).

Chapter 5

Gamma Rays from Clusters

Having discussed the basic constituents of the ICM and its observation through radio and X-ray, in this chapter we will return to the main subject of the thesis, by focusing on γ-ray emission in clusters. To that end we consider γ rays, as expected from interactions of CRs in the ICM and as indirect tracers of particle DM interactions.

5.1 CR-induced γ rays

Given the complex astrophysical environment, clusters provide ample possibilities to emit γ rays. First off, they are the host environments for AGNs which inject relativistic particles into the cluster medium throughout its lifetime. In fact, the only MeV-GeV detections of γ rays from clusters to-date concern their AGN origin, most prominently for instance γ-ray-emission from NGC1275 [152; 2; 39], IC310 [38; 129] and M87 [150; 34; 3]. It is important to point out that for an AGN origin, their γ-ray emission is expected to be point-like as far as the emission from individual objects is concerned. In the case of γ-ray emission from entire populations of AGN however, emission would be diffuse in nature making it difficult to distinguish it from the EGB (§3.3 for details).

On the other hand, the observed radio emission is inherently extended (see the discussion in the previous chapter). Comparing the typical lifetimes of CRes and CR protons (CRp) in the ICM (see Fig. 5.1), CRps accumulate throughout the formation of the cluster while CRes lose energy quite rapidly, resulting in much shorter lifetimes as compared to CRps. In order to produce the observed giant radio halos, CRes need to be either constantly replenished or re-accelerated (see, e.g. [66] for a recent review). In re-acceleration models, pre-existing CRe populations with $0.1 - 10\,\mathrm{GeV}$ are reaccelerated by plasma waves which are thought to be generated through turbulence that is induced during mergers (c.f.

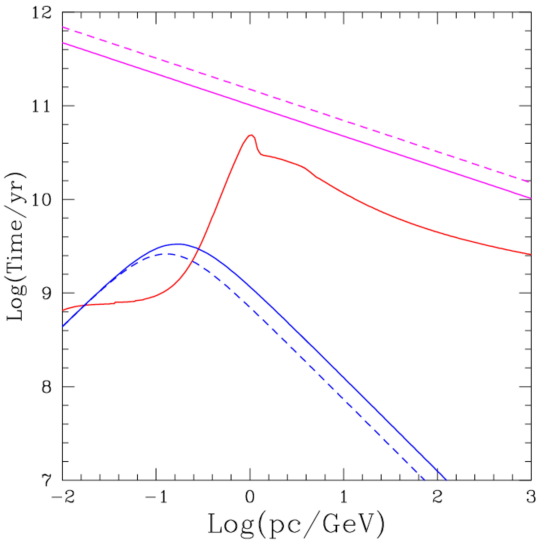

Figure 5.1. Compilation of CR lifetimes in the ICM at $z = 0$ (Figure credit: [55]). In blue, CRe are shown which lose energy at low momenta due to Coulomb cooling and at high momenta due to radiative losses. In red CRps are shown in comparison. The feature at $1 - 3\,\mathrm{GeV}$ in the time scale for CRps is due to a combination of shapes of the inclusive pp cross sections for π^+ and π^- [131]. The magenta line denotes the diffusion time for CRps assuming a Kolmogorov spectrum (see Blasi et al. [55] for the details of the diffusion model). Dashed lines correspond to a mean magnetic field of $3\ \mu G$ while solid lines are derived for $B \sim 1\mu G$. Even at the highest momenta, CRps are effectively confined within the ICM throughout the lifetime of the cluster.

[147; 69; 68; 134]). In this thesis we assume that the observed radio emission is in fact of secondary nature arising as by-product of (hadronic) interactions that produce charged and neutral mesons (primarily pions) which occur throughout the clusters volume (c.f. [82; 83; 84; 135]).[1] While the presence of CRps in clusters has not been detected directly in the ICM, the observations of CRs in our own galaxy suggest that CRes dwarf the contribution of CRps by more than two orders of magnitude (see, e.g. [153] for a review).

Depending on the magnetic field in the cluster, the CRes may also experience IC scattering with the surrounding radiation fields, most importantly the CMB and starlight in the cluster [112]. This process would then yield high

[1] We comment however on the observational constraints on turbulent re-acceleration models in the outlook (§7.2.1).

energy photons, primarily in the hard X-ray domain but possibly γ rays too. Spectrally, for the energy range probed with *Fermi*-LAT the resulting spectrum would then be a power law with a spectral index $-(\alpha - 1)/2$, where α is the index of the underlying CRe power-law spectrum [56]. On the other hand, a guaranteed signature of γ rays also arises from the decay of the neutral pions, i.e. $\pi^0 \rightarrow 2\gamma$, and the smoking gun for its detection would be the characteristic pion-decay bump, occurring at $\sim 67\,\mathrm{MeV}$, which is about half the rest mass of the π^0, $m_{\pi^0} \simeq 135$ MeV [132].[2] However, the potential γ-ray emission from clusters critically depends on the distribution of CRs.

In our own Galaxy, the engines that accelerate CRp to their highest observed energies $\sim O(\mathrm{TeV})$ are believed to be SNRs. Here, the CRps traverse the shock front from the SNR and are accelerated via first order Fermi-acceleration [116]. Typically, SNRs feature shocks with high Mach numbers ($\mathcal{M} \sim 100$) leading to an efficient acceleration of the CRs involving few crossings of the shock fronts [102]. Moreover, their function as hadronic accelerators has recently been observed through the *Fermi*-LAT discovery of the pion-decay cutoff spectrum in two nearby Galactic SNRs [18].

Based on the rate of SNs occurring in a cluster throughout its lifetime [97], one can thus estimate the number of remnants and by extension make predictions towards the minimum γ-ray emission from SNRs [165; 51]. In Paper IV we follow a similar approach to estimate the γ-ray emission we can expect from the Coma cluster under a minimal set of assumptions (see the discussion for details). Other than AGNs injecting high energy particles into the ICM, another potential energy source concerns the kinetic energy that is released during the formation of the cluster (such as during a major merger). Here, particle acceleration arises from diffusive shock acceleration (DSA) but the mach-numbers of the involved shocks are much weaker ($\mathcal{M} < 20$) than what is found in SNRs (see the discussion in appendix C in Paper I). Despite the lower mach numbers however, the collective effect of DSA is expected to be larger than that coming from AGNs or SNRs.

5.1.1 Universal CR model

The CR-based likelihood analysis carried out in Paper I and Paper II is based on the universal CR model put forward by Pinzke & Pfrommer [135], which we will discuss in brief in this Section. In their work the authors simulate 14 galaxy clusters in a cosmological environment, including shock acceleration as well

[2] Another potentially even cleaner signature would be the observation of neutrinos, which if detected, also can be used to point back to their origin of emission [171].

as injection of CR protons in high-resolution magneto-hydrodynamical simulations. In their sample they consider clusters with varying dynamical state that span over two orders of magnitude in cluster mass. The details of these simulation can be found in Pinzke & Pfrommer [135]. In brief the authors find that the resulting cosmic ray spectra from their individual clusters vary very little across their sample, indicating a spectrally universal model that is characterized by:

- a low momentum cutoff due to Coulomb cooling
- a concave shaped momentum spectrum ($p = 1 - 10^6$) with varying index $\alpha = 2.5$ at energies $\sim 1\,\mathrm{GeV}$ and $\alpha = 2.2$ at $\sim 100\,\mathrm{TeV}$ [3]
- a diffuse break towards high-momenta; the spectral index steepens by 0.3 and CRs above these energies can escape the clusters volume within the Hubble time

Within their simulations, they assumed a maximum hadronic injection efficiency, $\xi_{\mathrm{p,max}}$ of 50% due to DSA. This value is motivated by SNR observations, indicating $\xi_{\mathrm{p,max}} \geq 50\%$ [102]. Provided, we know the relation between the γ-ray-flux and $\xi_{\mathrm{p,max}}$, this presents a testable hypothesis using γ-ray data. In Fig. 5.2 we show the CR-induced γ-ray spectrum where two main features become apparent:

- Above $1\,\mathrm{GeV}$ the spectrum has a concave shape which may be approximated by a broken power-law over the energy range $1\,\mathrm{GeV} \leq E \leq 500\,\mathrm{GeV}$ with $\gamma_1 = 2.21$ and $\gamma_2 = 2.27$ where the break occurs at $\sim 10\,\mathrm{GeV}$
- At lower energies, the spectrum is characterized by a steeply falling part from $\sim 300\,\mathrm{MeV}$ down to $\sim 60\,\mathrm{MeV}$, with a peak in the γ-ray spectrum around the rest mass of the neutral pion.[4]

For a detailed discussion of the model, the reader is referred to Appendix B in Paper I and Pinzke & Pfrommer [135]. Another result of the simulation studies by Pinzke & Pfrommer [135] is that the volume averaged CR-to-thermal pressure ratio, $\langle X_{\mathrm{CR}} \rangle$ follows a simple scaling relation across their entire sample of simulated clusters (the reader is referred to the detailed discussion in Section 4.1 in Paper I). The universal CR model can thus be tested by introducing a

[3] Here p is defined as dimensionless CR momentum with $p = P_p/m_p c$ with P_p being the momentum of the CRs, m_p the protons mass, and c the speed of light.

[4] The underlying reaction is the interaction of two CR protons giving rise to pion-production as discussed in the previous section.

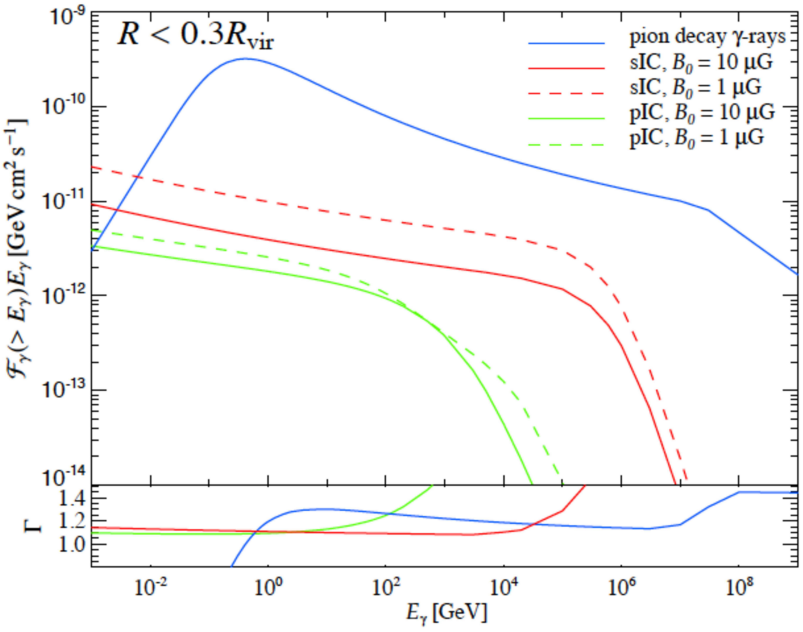

Figure 5.2. Shown is the predicted γ-ray spectrum from Pinzke & Pfrommer [135] (energy-weighted flux) over a wide energy range for a simulated Coma-like cluster, based on the universal CR model in the core region of the cluster $R < 0.3R_{\rm vir}$. The spectrum has been decomposed into the contribution of primary (green) and secondary (red) IC with different values of the central magnetic field (solid-line: $10\,\mu G$, dashed-line: $1\,\mu G$). Even in the outskirts, the authors find that the contribution from neutral pion decays dominates the resulting γ-ray emission, even though the difference between IC and the hadronic component is smaller. The lower panel shows the spectral index if a local power-law is assumed for the different components.

dimensionless scale parameter A_γ which, if the model holds, should be the same across the entire sample of studied clusters. Moreover, if one would measure $A_\gamma = 1$, this would mean that the observations match the model predictions [137].

In Paper I we show how a joint likelihood analysis (c.f. §6.3) can be used to constrain A_γ and in extension both $\langle X_{\rm CR} \rangle$ as well as $\xi_{\rm p,max}$. Note the strong underlying assumptions:

1. the γ-ray emission from all clusters can be modeled using the universal model
2. the scaling relations derived in Pinzke & Pfrommer [135] hold.

Moreover, if calculated for the entire sample of studied clusters, this also assumes that the values do not differ considerably between the morphological subsamples studied in Paper I (see below). By extension this method is applied to the case of the Virgo cluster (Paper II).

5.2 DM-induced γ rays

While we introduced the role of DM in the previous chapter as fundamental ingredient towards the formation of a cluster, we did not make any more statements regarding its exact nature. This thesis follows the assumption that DM is made up of weakly-interacting massive particles (WIMPs). One of the striking arguments in favor of WIMPs making up at least a part of the DM content of the Universe is sometimes referred to as WIMP miracle. In brief it can be shown that for a WIMP that was in thermal equilibrium with SM particles during early times and has freezed out and that is defined at the electroweak scale, the associated number density is approximately the same as what is needed in order to account for the cosmologically observed relic DM density. For these *thermal WIMPs*, the thermally averaged product of the cross section times the velocity is, $\langle \sigma v \rangle \sim 3 \times 10^{-26}\,{\rm cm^3\,s^{-1}}$. This value presents an important benchmark to compare experimental constraints with.

5.2.1 Search for WIMP DM

Generically speaking, the currently ongoing searches for WIMP DM can be classified into three distinct ways: the direct and indirect detection and the production of WIMPs in collider experiments.

Direct detection experiments work under the hypothesis a WIMP interacts with a target material which is traceable through the nuclear recoil of the target

nucleon (see, e.g. [50] for a review). The kinetic energy transferred is proportional to the mass of the WIMP, which a-priori is unknown. The biggest challenge with these kind of experiments concerns the identification of possible backgrounds, most importantly radioactive decays that may induce a false signal in the detector. Typically, these experiments are housed in deep underground laboratories in order to provide a sufficient shield to the contribution from CRs,

An alternative approach to the direct detection of WIMP DM is its production in colliders, such as the LHC. One major challenge arises from the fact that the WIMP does not leave any traceable detector signature behind thus one needs to rely on the full reconstruction of the underlying event and infer its contribution through the amount of missing transverse momentum in the detector (see, e.g. [44] for a recent review).

Finally, the third possibility of discovering DM is its indirect detection (see, e.g. [78] for a recent review). Here DM is expected to either annihilate or decay into (observable) standard model particles which can yield CRs, neutrinos and γ rays. On their path from the source to the observer the trajectories of (charged) CRs are altered due to the magnetic fields they encounter. Neutrinos and γ rays on the other hand travel in straight paths allowing to point back to their origin. Specifically, in the case of γ rays, the flux from the annihilation of a DM particle with mass $m_{\rm DM}$ can be written as:

$$\phi_s(\Delta\Omega) = \frac{1}{4\pi}\frac{\langle\sigma v\rangle}{2m_{\rm DM}^2} \times \sum_j B_j \times \frac{{\rm d}N_j(E)}{{\rm d}E} \times \underbrace{\int_{\Delta\Omega}\int_{l.o.s.} \rho^2(r) dl\, d\Omega'}_{\rm J-factor} \quad (5.1)$$

In the above equation we have introduced the thermally averaged product of annihilation cross-section times velocity, $\langle\sigma v\rangle$, the γ-ray yield ${\rm d}N_j(E)/{\rm d}E$ per final state j and the line of sight (l.o.s.) integral over the DM density. We refer to the latter as astrophysical or J-factor. A priori, the resulting continuum γ-ray spectrum is expected to be a superposition of different final states j with branching ratios B_j each having different γ-ray yields, ${\rm d}N_j(E)/{\rm d}E$. Being agnostic towards the possible annihilation signatures, for simplicity in this thesis we consider cases of pure annihilation into either quarks, leptons or W-bosons in order to bracket their potential γ-ray signatures (c.f. Fig 5.3).

Gamma Ray Lines

A special case concerns the annihilation (or decay) of DM into two photons (or $Z\gamma$, $h\gamma$, in which case a double-line is expected). In this case, the resultant

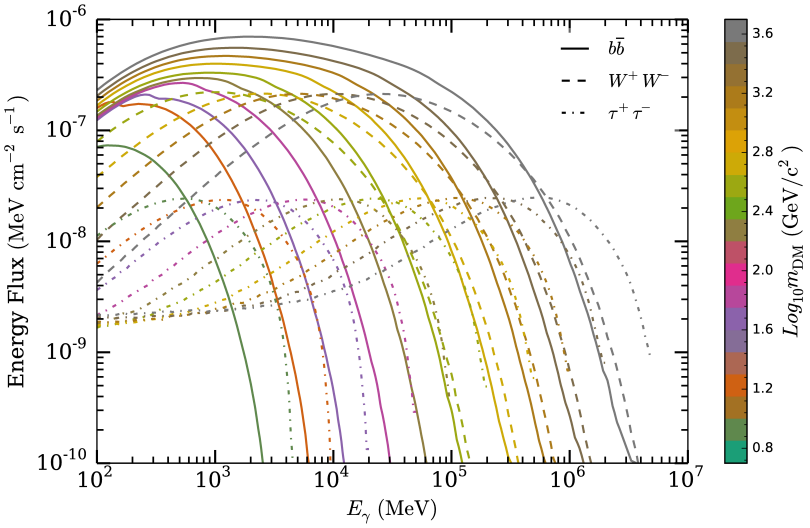

Figure 5.3. DM-induced energy flux spectra from WIMP annihilation into $b\bar{b}$ (solid), W^+W^- (dashed) and $\tau^+\tau^-$ (dash-dotted) for different WIMP masses (according to the color scale). All calculations were performed with DMFit as implemented in the *Fermi*-LAT ScienceTools [106; 22].

spectrum is a monochromatic line centered around the mass of the WIMP and Eq. 5.1 becomes:[5]

$$\phi_s(\Delta\Omega) = \frac{1}{4\pi}\frac{\langle\sigma v\rangle}{m^2_{\rm DM}} \times \int_{\Delta\Omega}\int_{l.o.s.} \rho^2(r) dl\, d\Omega', \tag{5.2}$$

Line-like features in the MeV-GeV energy range are considered a smoking gun signature since there exist no known astrophysical mechanisms that could produce lines at these energies.[6] Usually, this annihilation signature is however loop-suppressed making it a rare signal to search for [61].

The observation of a line-like feature towards the vicinity of the Galactic center observed with *Fermi*-LAT has recently attracted significant attention (see, e.g. [166; 154; 158; 59] for a very incomplete list), even though detailed follow-up investigations revealed that the significance of the detection has dropped greatly with respect to its first claims [20; 25]. In Paper III we address a claim related to the detection of line-like features towards the direction of the most nearby Galaxy clusters [101].

5.2.2 DM Distribution and Sub-halo Boost Factors

Returning to the J-factor in Eq. 5.1, this quantity is the line-of-sight integral of the DM density-squared ρ integrated over the solid angle $\Delta\Omega$. Navarro et al. [127] have shown that the DM density profile, $\rho(r)$, in galaxy clusters follows that of the universal Navarro-Frenk-White (NFW) profile [127; 128]:

$$\rho(r) = \frac{\rho_0 r_s^3}{r(r+r_s)^2}, \tag{5.3}$$

where we introduced r_s as the scale radius and ρ_0 as the characteristic (central) density of the profile. At this point it is worth pointing out that while Eq. 5.3 may suggest that DM is present as one large smooth halo, cosmological N-body simulations indicate that DM in fact tends to cluster - into smaller sub-halos of varying size (and numbers), both quantities which are poorly constrained by data and thus highly uncertain. The minimum size of DM sub-halos, $M_{\rm cut}$ may be as low as $10^{-6}\,M_\odot$ [98; 139] which is far below the current resolution limit of cluster-size N-body simulations ($10^8\,M_\odot$) [94]. To estimate the concentration, c, of DM sub-halos, and thus to describe the internal structure of these

[5] For the case of annihilation into $Z\gamma$ and $h\gamma$ if one line is expected at an energy E, the second line is expected to occur at $E' = E\left(1 - \frac{m^2}{4E^2}\right)$ where m is the mass of the Z/h respectively.

[6] See however, [32] for a recent astrophysical explanation of O(100 GeV) γ-ray lines via ultrarelativistic pulsar winds.

objects, extrapolations of the mass-concentration relation, $c(M)$ are required that span several orders of magnitude (here we introduced c as concentration parameter). Earlier works advocated to assume a power-law extrapolation of the $c(M)$ relation towards $M_{\rm cut}$ [94; 93]. This picture has started to change gradually, with recent works showing that $c(M)$ flattens towards the smallest halo masses, clearly rejecting the earlier power-law extrapolations [146]. Returning to Eq. (5.3), we can express ρ_0 and r_s in terms of c:

$$\begin{aligned} r_s &= r_{200}/c \\ \rho_0 &= \frac{200}{3} \times \frac{c^3 \times \rho_c}{\ln(1+c) - c/(1+c)}, \end{aligned} \tag{5.4}$$

connecting the virial radius, r_{200}, with the scale radius and the central density with the critical density of the Universe. The J-factor for $r < r_{200}$ at a large angular distance, D_A (typically $O(100)\,{\rm Mpc}$) can then be approximated by:

$$J_{\rm NFW} = \frac{4\pi}{3} \rho_0^2 r_s^3 \frac{1}{D_A^2} \propto \frac{c^3}{f(c)^2} \tag{5.5}$$

Thus, the value of the concentration parameter has a crucial impact on the predicted J-factor, and by extension on the predicted total γ-ray annihilation flux which may be largely enhanced if substructure is taken into account [136; 94; 93].[7] With $L_{\rm NFW} = 4\pi \times \phi_s \times D_A^2$ being the luminosity of the smooth NFW halo (inserting the J-factor from Eq. 5.5 into Eq. 5.1), in the following we adopt the DM annihilation flux profile in clusters from detailed N-body simulations [94] that gives a parametrization in terms of the projected luminosity profile $I_{\rm sub}(\theta)$ at an angular radius $\theta < \theta_{200}$:

$$I_{\rm sub}(\theta) = \frac{16 b \times L_{\rm NFW}}{\pi \times \ln(17)} \frac{1}{\theta_{200} + 16\theta^2}. \tag{5.6}$$

In the above equation we have introduced b as the *boost* factor that contains the enhancement in terms of DM substructure. Since Eq. 5.6 is given in terms of θ, we introduced $\theta_{200} = \arctan(r_{200}/D_A) \times 180^\circ/\pi$ which is the subtended angle corresponding to r_{200} (which in this thesis we sometimes refer to as angular virial radius). The research presented in this thesis reflects the ongoing debate on DM substructures and while we consider a consistent minimum cut-off scale of $M_{\rm cut} = 10^{-6} M_\odot$, in Paper II and Paper III we derive our results within both scenarios, where the power-law extrapolation scheme leads to an

[7] For decaying DM this problem is much less important since the corresponding J-factor is a linear integral over the DM density instead.

optimistic prediction as the boost factor $O(1000)$ becomes large and contrast our findings with the more recent considerations by Sánchez-Conde & Prada [146] giving a more *conservative* estimate of $b \sim (30 - 100)$ for cluster-size halos. Both models share the prediction of enhanced γ-ray emission in particular towards the outskirts of the cluster. We remark that Sánchez-Conde & Prada [146] do not provide a direct parametrization of the flux annihilation profile but earlier works using this approach confirm its flattening towards the outskirts of the cluster [138]. Hence, we assume Eq. 5.6 to be valid for both of our scenarios and distinguish them only by their respective values of b. In Fig 5.4, we show how the boost-factor relates to the virial mass, M_{200} (c.f. §4.2) along with the resulting flux annihilation profiles for the Virgo cluster to illustrate the differences.

For the mass estimate of the clusters we studied in this thesis we use mass measurements from the ROSAT X-ray telescope [142; 75] which are however not measured beyond r_{500} [R. Rotshild, private communication]. For a given model for $c(M)$, we can numerically obtain the value for M_{200} for the reported set of values of $\{M_{500}, r_{500}\}$ that satisfies the integral over $\rho(r)$ from Eq. (5.3): $M_{500} = \int_0^{r_{500}} \mathrm{d}^3 r\, \rho(r)$.

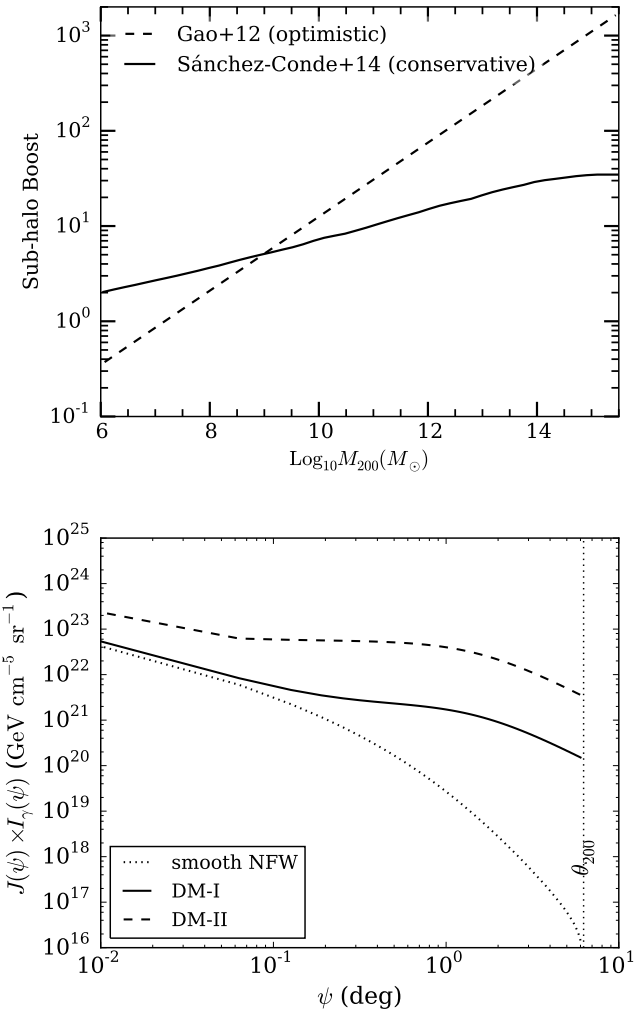

Figure 5.4. *Top*: Comparison of different sub-halo boost factor models. The dashed line corresponds to earlier (now disfavored) power-law extrapolations [94] whereas the solid line correspond to the model put forward by Sánchez-Conde & Prada [146] (figure adapted from [146]). *Bottom*: Shown is the annihilation flux profile as function of subtended angle ψ on the sky for the Virgo cluster (figure taken from Paper I). The dotted line corresponds to the case where no substructure is included. Solid and dashed lines correspond to the conservative and optimistic configurations, as discussed in the main text. Beyond the virial radius we truncate the contribution to the profile.

Chapter 6

Data Analysis and Likelihood Method

In this chapter we discuss the common data analysis techniques and introduce the terminology used throughout the papers contained in this thesis. We denote standard tools that are also available for public use (distributed as Fermi-LAT ScienceTools) in `typewriter font`.

6.1 LAT likelihood analysis

Here we outline the typical chain from the photon-level event file to calculating constraints on physical parameters of interest. We show a schematic view of the analysis flow in Figure 6.1.

The starting point are the publicly available photon list and the spacecraft file. The former, which we refer in this work as ft1 or event-level file contains the arrival times of each photon along with its direction in the sky and its reconstructed energy. A number of auxiliary quantities is also provided which allow the sub-selection of photons according to quality cuts. The spacecraft or ft2-file contains information about the state of the spacecraft, whether or not it was in pointed or survey (nominal) operation mode and is used to identify good time intervals (GTIs), using the `gtmktime` tool which are used for the further analysis. Photon data selection is done using `gtselect` in which the user defines circular regions of interest (ROIs) around their target of interest which define the region in which photons are selected. In order to evade the strong emission from the bright Earth limb, we usually employ a cut on the zenith angle of the spacecraft, $z_{\rm max}$. Also in order to both minimize limb emission and to provide uniform sky exposure, the LAT "rocks" back and forth, with a typical rocking

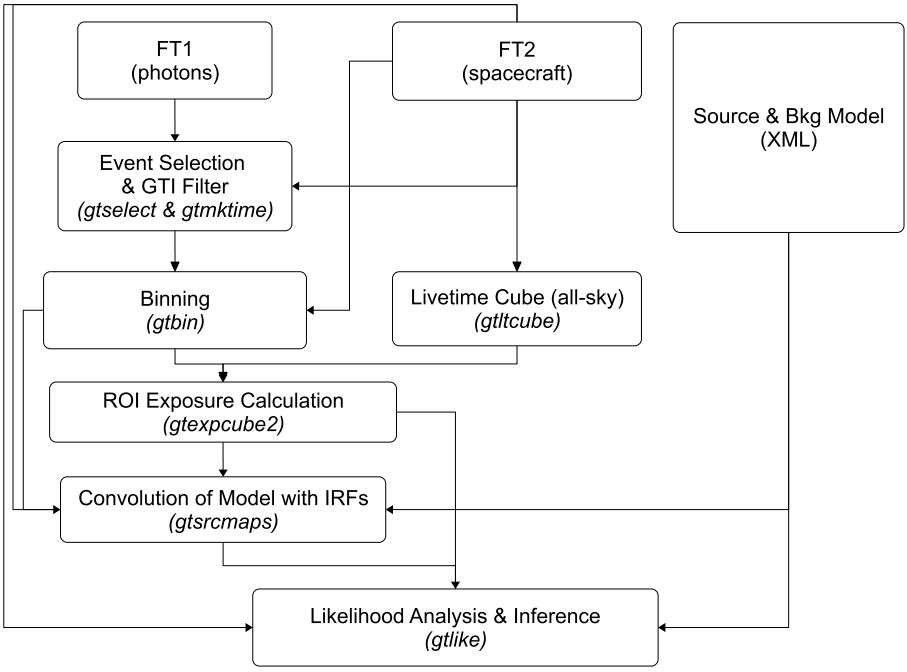

Figure 6.1. Schematic view of the binned LAT analysis in *Fermi*-LAT. Tools are marked in italics.

angle profile of $\sim 50^{\circ}$ (c.f. §2.1), which is accounted for in the analysis by demanding events to be selected that fall within both the $z_{\mathrm{max}}$and the rocking angle cuts (refer to Fig. 6.2 for the definition of these angles with respect to the observatory). For typical ROIs with radii of $\sim O(10^{\circ})$, the exposure varies only marginally, especially when considering the long integration times in this thesis. In order to compute the exposure E, we use the `gtltcube` tool which provides an all-sky exposure 'cube' depending on the zenith angle and rocking angle profile used. Data binning is done using `gtbin` in which the number of spectral and spatial bins is determined. The output most suitable for the analyses presented here are counts cubes which are two-dimensional projections of the incoming photons per slice for each energy bin. Together with the model cubes that are obtained by forward-folding the input model with the instrument response with `gtsrcmaps` (c.f. §2.3.2), these are the quantities used in the maximum likelihood analysis that is presented as follows.

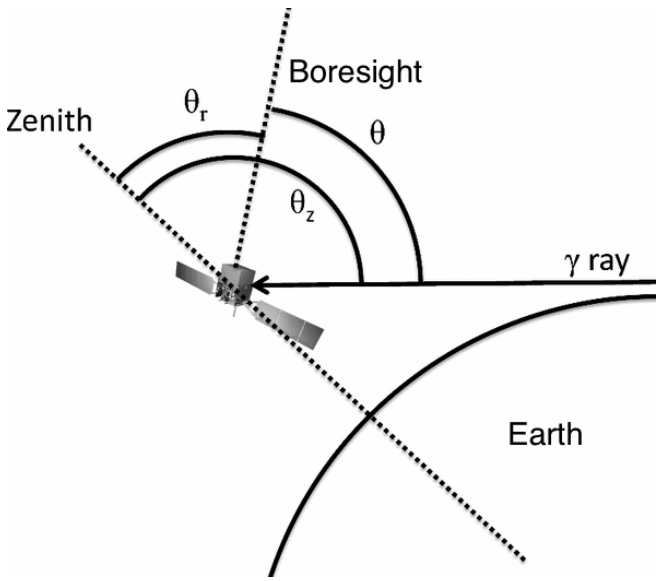

Figure 6.2. Schematic overview of the most important angles, adapted from [20]. θ refers to the incident angle of the incoming photon while θ_r and θ_z denote rocking and zenith angle, respectively. Photons entering the boresight of the LAT are sometimes referred to as entering at *normal incidence*.

6.1.1 *Fermi*-LAT Likelihood

Let the number of predicted photon counts in bin i in $(E, \mathbf{x})$ be μ_i, where E is the photon energy and $\mathbf{x}$ its direction. The probability p_i to observe n_i counts in bin i is then given by the poisson distribution:

$$p_i = \mu_i^{n_i} \frac{e^{-\mu_i}}{n_i!} \tag{6.1}$$

The likelihood is the product of all p_is for all bins, thus:

$$\mathcal{L}(\mu|n) = \prod_i \mu_i^{n_i} \frac{e^{-\mu_i}}{n_i!} = \prod_i e^{-\mu_i} \times \prod_i \frac{\mu_i^{n_i}}{n_i!}. \tag{6.2}$$

Note that μ_i is a function of the source model $S(E, \mathbf{x})$. This source model contains both point-like and diffuse sources, so one can write

$$S(E, \mathbf{x}) = \sum_i S_i(E, \mathbf{x}). \tag{6.3}$$

Assuming that one can separate spatial and spectral part from one another, for a point-like source, S_i is:

$$S_i = \tilde{S}_i(E)\delta(\mathbf{x} - \mathbf{x_i}). \tag{6.4}$$

This source model is convolved with the instrument response introduced in Chapter 2.3.2 (refer to Eq. 2.1 for details) and μ_i is then given by:

$$\mu_i = \int_i dE' d\mathbf{x}' \int_{SR} dE d\mathbf{x} R(E', \mathbf{x}'; E, \mathbf{x}) S(E, \mathbf{x}). \tag{6.5}$$

In the above equation, $\int_i dE' d\mathbf{x}'$ refers to the integral over the i-th bin and $\int_{SR} dE d\mathbf{x}$ denotes the integral over the *source region*, which extends over all energies and in principle the entire sky.

Using $\prod_i e^{-\mu_i} = e^{-\sum_i \mu_i} = e^{-N_{\mathrm{pred}}}$, where N_{pred} is the total number of *predicted model counts* and taking the logarithm of Eq. 6.2 gives the usual form of the log-likelihood function that is to be maximized:

$$\log \mathcal{L}(\mu|n) = -N_{\mathrm{pred}} + \sum_i n_i \times \log \mu_i. \tag{6.6}$$

Note that in Eq. 6.6 we omitted a term $-\log n_i!$ which relates to the data. This term is independent of the model parameters and does not change during the optimization step, hence contributes as a constant offset.

The public tools provided by the LAT collaboration allow for photon analysis in two distinct ways: one in which both spatial and spectral information is binned (binned analysis) and one in which the spectral information is retained by using the full unbinned information regarding the energy of each reconstructed photon (unbinned analysis). The majority of the works presented in this thesis employ the former while Paper III uses an unbinned maximum likelihood method instead. Since the preparation steps are different for unbinned analyses, the reader is referred to § 2 of Paper III for details. Per default the Science Tools do not provide means to include the energy dispersion in the unbinned likelihood analysis. Thus in order to account for its non-negligible effect in searches for monochromatic lines in Paper III we first simulated photons according to a monochromatic line and used the resulting sampled spectrum in our analysis.

Due to the different response, LAT analysis is performed separately for front- and back-converting events (see the discussion in §2.3). With Pass 8 this concept was extended to consider event types. Here the analysis is done for each event type separately and combined afterwards.

6.2 Hypothesis Testing and Confidence Intervals

The likelihood function defined in Eq. 6.6, can be used for statistical inference. In this thesis we consider two applications: testing the hypothesis of an additional signal s above background b and for the calculation of confidence intervals, for instance on s. Let us consider two hypotheses, the null-hypothesis H_0 with the maximum-likelihood value $\mathcal{L}(s = 0, \hat{\hat{b}})$ (with $\hat{\hat{b}}$ being the maximum likelihood estimate (MLE) for the null hypothesis) and the alternative hypothesis H_1 with $\mathcal{L}(\hat{s}, \hat{b})$. We can define a test statistic TS, which is the ratio of these two likelihood values [120]:

$$TS = -2 \log \left(\frac{\mathcal{L}(s = 0, \hat{\hat{b}})}{\mathcal{L}(\hat{s}, \hat{b})} \right) \tag{6.7}$$

To obtain the significance, N_σ associated with the best fit MLE on the signal strength $\hat{s}$, we can integrate the null-distribution to the desired value of TS to obtain its associated p-value. N_σ is then given by:

$$N_\sigma = \sqrt{2} \mathrm{erf}^{-1}(1 - p), \tag{6.8}$$

where erf^{-1} is the inverse error function. We expect the null-distribution of TS to be distributed as χ^2_k (Wilks theorem, [169]) and if we constrain s to be positive definite, to be distributed as $\frac{1}{2}\delta + \frac{1}{2}\chi^2_k$ (Chernoff's theorem, [76]) with

k degrees of freedom. Under this assumption we can relate the significance of the source (in units of σ) with signal strength MLE $\hat{s}$ to be $N_\sigma = \sqrt{TS}$ [120]. For a detection we typically consider a 5σ detection threshold or a p-value of roughly 10^{-7}, which translates to $TS = 25$. We have explicitly verified that the null distribution in MC simulations follows a χ^2 distribution as per Chernoff's theorem. A data-driven approach to obtain the null distribution is however to take *blank fields* from the measured γ-ray sky instead (as in Paper IV).[1] Due to the presence of sources that are yet unresolved by the LAT (c.f. §3.3), we expect a departure from this idealized case (see, [22] for a discussion). The null distribution may also be affected by correlations in the target region (c.f. 6.5).

We also introduce a related quantity, $TS_{\rm ext}$ which we use to test whether or not a source is spatially extended [114]:

$$TS_{\rm ext} = 2\log\left(\frac{\mathcal{L}_{\rm ext}}{\mathcal{L}_{\rm PS}}\right) \tag{6.9}$$

where $\mathcal{L}_{\rm ext}$ refers to the maximum-likelihood value with an extended source hypothesis and $\mathcal{L}_{PS}$ is that associated with a point-source hypothesis. Lande et al. [114] has shown through MC simulations that the null distribution of $TS_{\rm ext}$ follows Chernoff's theorem for extensions $R \geq 0$ up to some minor discrepancy with some simulation setups tending to yield lower than expected values of $TS_{\rm ext}$. Consequently, Lande et al. [114] adopted a formal threshold of 4σ or $TS_{\rm ext} = 16$ when testing a potential γ-ray source for extension. We follow this recommendation and adopt the same threshold value.

6.2.1 Confidence Intervals

For confidence intervals, we wish to estimate the interval $[s_{ll}, s_{ul}]$ which contains the true value $s_{\rm true}$ at a given probability α. Typically, we are interested in the upper limits on the signal strength s at a given confidence level α. Generically, the background model is more complex, thus we consider $\mathbf{b}$ to be a vector containing different background (nuisance) parameters. We choose to use the profile likelihood method [49; 143] and on a technical level its implementation in the MINUIT package, MINOS [105]. Specifically, we maximize $\mathcal{L}$ for each value of s with respect to $\mathbf{b}$. In the case of one free parameter, the 95% C.L. one-sided upper limit on s, s_{ul} is given by:

$$\log\mathcal{L}(s = s_{ul}, \hat{b}) - \log\mathcal{L}(s = \hat{s}, \hat{b}) \stackrel{!}{=} 2.71/2. \tag{6.10}$$

[1] We define a blank field by a patch in the sky whose central coordinate does not coincide with a previously detected xFGL source or cluster (as taken from the HIFLUGCS catalog).

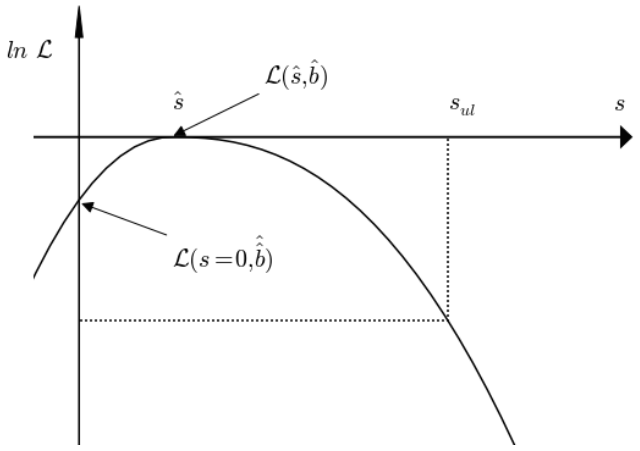

Figure 6.3. Schematic example of profile (log)-likelihood for the signal parameter s. The dotted horizontal line corresponds to the visualization of s_{ul}.

In Fig. 6.3 we show schematically the different quantities introduced in this section.

6.3 Joint Likelihood & Applications

In the cases studied in this thesis, often we expect the signal to be too faint to be detected in a single source. In order to increase the statistical significance one can then try to stack several sources on top of each other. Joint likelihood is such a source stacking technique, in which the likelihood function for each ROI is maximized individually while having one ore more common parameters tied across all corresponding likelihood functions. Following the previously introduced notation, the joint likelihood can be written as product of all individual source (ROI) likelihoods $\mathcal{L}_i(s, \mathbf{b_i}|\mathrm{obs}_i)$:

$$\mathcal{L}(s|\mathrm{obs}) = \prod_{i}^{\mathrm{ROIs}} \mathcal{L}_i(s, \mathbf{b_i}|\mathrm{obs}_i) \tag{6.11}$$

The same construction can be used when having multiple sources in one ROI (as it is the case in Paper I). Under this assumption, that there is a common parameter in a target model that is expected to be the same for various targets, this method allows for a more robust determination of parameters and provides more stringent constraints as the combined constraints will typically depend less

on individual fluctuations in each ROI. Originally it was used to determine the DM annihilation cross-section in a combined analysis of local dwarf galaxies [14; 22] but has since been extensively used. In the context of this thesis, joint likelihood is used in various flavors:

- Paper I introduces a common scaling parameter which is related to the maximum hadronic injection efficiency due to large scale structure formation shocks (c.f. §4.1.1) Note that in addition it uses multiple targets per ROI (in contrast to the other works considered in this thesis).

- Paper III uses the joint likelihood method in the context of DM searches

- Paper IV employs an extension of joint likelihood which we refer to as bin-by-bin likelihood (see §6.4).

The remainder of this chapter outlines this method and discusses some of its advantages over other forms of combining multiple datasets (stacking).

6.3.1 Common Parameters of Interest

The application of joint likelihood is useful if one can express the target model of interest in terms of a common parameter. For DM studies, such as Paper II or Paper III its identification with the annihilation cross-section is straightforward since we expect DM to be present universally on various scales (from interactions in our local neighborhood to cluster-size halos, see the discussion in Chapter §5.2.2). The joint likelihood in the case of DM (see, e.g. Paper II) can be written as:

$$\mathcal{L}(\langle\sigma v\rangle, m_\chi|\mathrm{obs}) = \prod_i \mathcal{L}_i(\langle\sigma v\rangle, m_\chi, J_i, b_i, c|\mathrm{obs}_i) \tag{6.12}$$

In the case of the log-likelihood, the product is replaced by a sum over all ROIs. Here m_χ is the mass of the DM particle and $\langle\sigma v\rangle$ the velocity-weighted average annihilation cross section (or the decay time, τ), both parameters of the model which we want to use for inference. J_i refers to the astrophysical J-factor introduced in §5.2.2, which serves as weighting factor (see §6.3.2), since the flux is proportional to J. The individual $\mathcal{L}_i$ are dependent on individual model parameters, e.g. for background point-like sources, denoted by b_i or overall constants c. Here the index i runs over each considered target source in the ROI.

In contrast, in Paper I we set out to constrain the dimensionless quantity A_γ which can be related to both $\langle X_{\rm CR} \rangle$ and under suitable assumptions to $\zeta_{p,\rm max}$ (see discussion in § 5.6 in that paper and §5.1.1).[2] Thus, eq. 6.11 becomes:

$$\mathcal{L}(A_\gamma|\rm obs) = \prod_i \mathcal{L}_i(A_\gamma, b_i, c|\rm obs_i) \tag{6.13}$$

where A_γ is the common parameter we wish to constrain. In contrast to Eq. 6.11, here the index runs over all ROIs and each individual likelihood is actually constructed as a joint likelihood function, extending over j sources. Thus, the ROI likelihood function over j sources is given by:

$$\mathcal{L}_i(A_\gamma, b_i, c|\rm obs_i) = \prod_j \mathcal{L}_j(A_\gamma, F^{\rm CR}_{\rm exp,j}, b_i, c|\rm obs_i) \tag{6.14}$$

In the above equation, we also have $F^{\rm CR}_{\gamma,\rm exp}$, denoting the CR-induced γ-ray flux for each cluster (see the detailed description in §5.1.1). The nuisance parameters b_i and c are determined for the entire ROI.

The above approach can be generalized to the concept of event types where we replace the product that runs over individual ROIs with one that iterates over different event types [25].

6.3.2 Weighting

One advantage of having a complex likelihood function such as the one introduced in the previous section is the ability to encode additional information regarding each target in the likelihood function along with its potential uncertainties. More specifically, the clusters mass, its distance (or redshift) and other key parameters determine how much each target individually contributes to the overall flux. In all cases studied in the accompanying papers we encode this information into a single parameter: $F^{\rm CR}_{\gamma,\rm exp}$ in Paper I and II, and the J-factor in Paper II and III. Since $\phi_\gamma \propto F^{\rm CR}_{\gamma,\rm exp}$ and $\phi_\gamma \propto J$, these parameters serve as a weighting factor in the joint likelihood.

Thus, ROIs that contain targets which for the case of DM have a large J-factor (or for CR large $F^{\rm CR}_{\gamma,\rm exp}$), contribute more in the joint likelihood, than ROIs containing targets with smaller J-factors. In the case of e.g. an excess that is observed in a cluster that has a relatively low J-factor, this implies that the overall contribution becomes small, further penalizing individual excesses

[2] In principle this quantity is constructed such that $A_\gamma = 1$ corresponds to observations which are consistent with the predictions by Pinzke et al. [137].

which may be due to overfluctuations which are however not in accordance with the expectations of the model.

In all cases we studied we neglected the intrinsic uncertainties on the aforementioned cluster parameters such as mass, distance or the resulting J-factor. The latter is further motivated by the fact that the largest uncertainty in determining the J-factor is the amount of substructure (c.f. §5.2.2), which may change the J-factor by orders of magnitude. Instead of including this uncertainty we chose to instead pick bracketing cases of substructure configurations rather than including a term in the likelihood that encompasses these uncertainties.

6.4 bin-by-bin Likelihood

One challenge with the applications of the joint likelihood approach as discussed in §6.3 is that the likelihood function needs to be modified (and maximized) whenever the model is changed. A priori there is no preference for a specific final state for DM to annihilate into for instance, requiring a full likelihood analysis for each tested model. This can be alleviated if it were possible to identify a spectrally model-independent representation whose likelihoods can then be combined a-posteriori. Developed for the search for DM-induced γ rays in dwarf galaxies, the bin-by-bin likelihood provides this representation [86; 22]. Assuming a single power-law in each energy bin for a putative γ-ray source, the only remaining free parameter is the normalization of the power-law, denoted μ_i. The bin-by-bin profile likelihood can then be written as $\mathcal{L}_i(\mu_i, \hat{\theta}|\mathrm{obs}_i)$ where $\hat{\theta}$ indicates that the nuisance parameters θ have already been profiled over. This representation can be directly used to test a variety of spectral models given the normalization $\mu = \mu_i$ and the full likelihood is formed yet again by joining (this time the bins):

$$\mathcal{L}(\mu, \hat{\theta}|\mathrm{obs}) = \prod_{i}^{\mathrm{bins}} \mathcal{L}_i(\mu_i, \hat{\theta}|\mathrm{obs}_i). \tag{6.15}$$

One immediate advantage is that in addition to model-specific constraints, these profile likelihoods can be published in a suitable form and different spectral models (and spatial models if applicable) can be tested easily without the need for a repeated likelihood analysis.

6.5 Correlations and Blank Fields

The use of joint likelihood as defined in eq. 6.11 does not account for correlations between the $\mathcal{L}_i$. This is generally true for combinations of observations

where the different targets are far away from one another and do not share the same ROIs. The extensive tails in the PSF make the definition of *observations being uncorrelated* difficult however. Correlations, or more specifically overlap can occur both for targets and background sources.

The latter is less critical since each ROI is optimized individually and for computational reasons, the background sources are fixed to their best-fit values prior to combining them. The contributions from both Galactic and Isotropic diffuse are expected to be correlated on large scales, and are allowed to be refitted. However, they are evaluated by optimizing the entire ROI in each case, thus partial overlap is less hazardous.

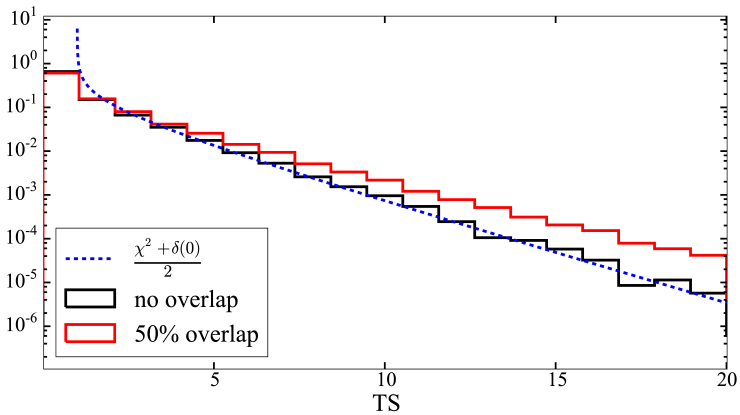

Figure 6.4. Shown is the null distribution of TS as defined in Eq. 6.7 when considering no overlap in the target (black) and when 50% of the photons are shared. The dashed blue line corresponds to the theoretical prediction according to Chernoff's theorem. Figure from Anderson et al. [41].

Overlap in the target region by e.g. considering a merging cluster system such as defined by the clumps around M49 and M87 as discussed in Paper II by analyzing two separate ROIs, one centered on M49 and one on M87 and combining those can lead to substantial biases (see the discussion in a simplified scenario in §A.1 of Paper I and also [41]). Moreover, target overlap will also contribute to deviations in the TS null distributions (c.f. Fig 6.4). Thus, when constructing the previously mentioned blank fields in the sky, overlaps in the target region needs to be considered as well. For instance, if one considers the high-latitude sky and removes spots that are occupied by point sources, one is left with about 3.3 sr blank fields. This number can then be used to estimate the number of uncorrelated blank fields given a considered emission region.

6.6 Sliding Energy Window

In the preceding chapter we have considered a binned likelihood analysis both in spatial bins (pixels) and energy bins. While we find that the specific choice of binning has a minor impact on the results presented both in Paper I and Paper IV, when searching for monochromatic line features (see §5.2.1) an unbinned likelihood analysis is desired as the binning can wash out features.[3] In order to identify typically small local excesses on top of a dominant powerlaw background, we can instead use a sliding energy window (see, e.g. [7; 166; 20]). To this end we partition the entire spectrum into smaller parts (windows) which are locally fit to a power-law and a line. It is convenient to express both null hypothesis, H_0, (power-law background) and alternative hypothesis (line on top of power-law background), H_1:

$$\begin{aligned} H_0 &= B(N_0, \Gamma) \\ H_1 &= B(N_0, \Gamma) + G(N_{\rm DM}, E_\gamma). \end{aligned} \tag{6.16}$$

Here B denotes a power-law spectrum whose free parameters (to be determined in the fit) are the normalization N_0 and the (local) power-law index Γ. $G(E_\gamma, N_{\rm DM})$ denotes a Gaussian with a negligible width $\sim$ GeV centered at the line energy E_γ and scaled with the normalization $N_{\rm DM} = \frac{J \times \langle \sigma v \rangle}{4\pi \times m_{\rm DM}^2}$ (see Eq. (5.2)). We perform a maximum likelihood fit for each energy window. The resulting free parameters are N_0, Γ, and $N_{\rm DM}$. In addition, in Paper III we also allow hard sources with $TS \geq 100$ (10σ) for $E \geq 10\,{\rm GeV}$ to vary in their respective normalization in order to account for variability of these sources.[4] At most this introduces 4-5 additional free parameters per ROI.

When determining the optimal window size, we considered two choices 6σ and 12σ where σ refers to 68% quantile of the energy dispersion $D(E_\gamma)$ (c.f. §2.3.2). We decided to pick 6σ because the larger window was too computationally challenging (in addition to the large ROIs) when confronting a simulation of a monochromatic line in addition to a realistic background as generated by `gtobssim`.

[3] Specifically we are considering line features where the resulting line width is smaller than the energy dispersion at the given line energy $\sim O(\text{few})\text{GeV}$.

[4] When analyzing LAT data we take the most current catalog of detected LAT sources and include them in our background model. Since these catalogs are not continuous but refer to fixed durations, such as 1 year for 1FGL, 2 years for 2FGL, etc. the best-fit parameters from the original analysis period considered in each catalog may have changed. To account for this we typically leave the brightest sources free to vary in the likelihood fit.

Another challenge arises through the fact that the energy windows are typically correlated with one another, at least if neighboring windows are considered. We correct for this effect by calibrating the resulting TS distribution (with TS being the likelihood ratio of H_0 and H_1) based on background-only MC simulations (c.f. §3.1, Paper III).

Chapter 7

Discussion of Results, Summary and Outlook

7.1 Discussion of Results & Summary of Papers

The main message that all accompanying papers in this thesis convey is that there is no significant evidence for γ rays from Galaxy clusters that can be associated with the most massive nearby clusters. More specifically, in this section we briefly summarize the main findings of the various papers.

Paper I

We have performed a joint likelihood analysis of a subset of 50 nearby galaxy clusters searching for extended γ-ray emission using four years of LAT survey data. With the exception of individual excesses in three clusters: Abell 400, Abell 1367 and Abell 3112 we find no evidence for γ rays that can be attributed to the cluster. In regards to the aforementioned individual clusters, we find sufficient support that the γ-ray excess instead originates from previously not-detected point sources that may be cluster member galaxies or other background sources. The most significant of the excesses is towards Abell 400 which in our model has small flux expectation compared to larger clusters such as the Coma cluster but exhibits an excess at a significance of $6.7\,\sigma$ (see Section 5.3 in Paper I). Note that since the predicted flux of Abell 400 is much smaller due to its distance and mass (as compared to for instance the Coma cluster), its relative contribution to the joint likelihood is small as well.

In a similar recently published analysis [140], the authors claim a 4.7σ excess after having analyzed a similar amount of data and using a similar sample, which is in tension with the findings reported in our paper. This tension

can however be alleviated considering that the authors assume equal weights in a data-stacking approach instead. This exemplifies the importance of existing prior information on cluster parameters, such as mass and distance which are treated coherently in the likelihood analysis.

We remark that while the analysis reported in our paper used four years of *Fermi*-LAT exposure, the available catalog of point sources was based on two years and the most significant excess reported in Paper I is actually found to be spatially coincident with a new 3FGL source, 3FGL J0258.9+0552, which however has no listed association with sources reported in other wavebands. In the subsequent catalog search the source is reported with a best fit power-law with $\Gamma = 2.1$ and an average reported significance of 7σ [10].

We leave the reported excesses unmodeled and conservatively calculate flux upper limits on the γ-ray emission under the assumption of the universal CR model by Pinzke & Pfrommer [135]. Using the joint likelihood approach discussed in §6.3 we constrain the maximum injection efficiency, $\zeta_{p,\mathrm{max}}$ of CRp due to DSA to be less than 21% (which at the time were the most stringent upper limits). The same constraint can also be taken to limit the volume-averaged CR-to-thermal pressure ratio, which we find to be below 1.25% and 1.4% depending on whether we consider cool-core or non-cool-core clusters or the entire sample. At the same time we reject the flux predictions based on the model by Pinzke & Pfrommer [135] at the 5σ-level if the entire sample of clusters is concerned.

Paper II

This paper is mainly a systematic investigation of earlier claims of very extended γ-ray emission from the direction of the Virgo cluster [99; 119]. Due to its proximity, the Virgo cluster appears as much larger object on the sky, subtending around 14° across the sky. As such this target is particularly challenging especially given the large uncertainties associated with the diffuse γ-ray foreground modeling. The paper aims to provide a coherent investigation in which we report a faint excess of diffuse nature. In this paper we discuss how the aforementioned uncertainties can be quantified by using alternative diffuse models as proxy. We account for part of the excess by introducing new point sources in the region (which are in part solid detections reported in 3FGL) and develop an improved foreground model for the region.

The Virgo cluster is in fact undergoing a large merger, mostly driven by the motion of the sub-cluster centered on the giant elliptical galaxy M49 towards the main clump that can be associated with M87. For the first time we account for this merger and model the predicted γ-ray profiles as superposition of the two subsystems. To provide constraints on CR physics we consider the same

scenario as the one studied in Paper I. However, due to the excess emission we find comparatively low limits of $\zeta_{p,\mathrm{max}} \leq 40\%$ and $\langle X_{\mathrm{CR}} \rangle \leq 6\%$. Lastly, since the initial claims based on Virgo favored a DM-origin over that of CR physics, we derive limits on the DM annihilation cross section considering two benchmark models (§5.2.2) addressing for the additional contribution from DM sub-halos, finding limits that are roughly an order of magnitude above that of a thermal relic.

Paper III

As discussed in this thesis, a few years ago claims were made of having detected a significant amount of monochromatic γ rays from the direction of the Galactic center [166; 154; 158; 59]. In addition other targets were studied and this paper addresses a so-far undisputed claim of evidence for γ-ray lines with $E \sim 130\,\mathrm{GeV}$ originating from the most nearby Galaxy clusters [101]. We used an unbinned maximum likelihood analysis employing the full spatial information in regards to the possible γ-ray annihilation signature and a sliding window to search for features in five years of high energy ($E \geq 10\,\mathrm{GeV}$) photons collected by the LAT. While we find no statistically significant evidence, we note a double-bump structure when comparing our observed limits with the expected sensitivity evaluated based on MC simulations, which however falls within the 68% and 95% containment bands evaluated from realistic MC simulations. Furthermore we find that the local significance in the claimed energy regime ($E \simeq 130\,\mathrm{GeV}$) decreases, supporting the hypothesis of a statistical fluctuation.

Paper IV

In this paper we use the latest set of reconstruction tools distributed as *Pass 8* to study the Coma cluster, which is among the best studied systems due to the large amount of available contemporary multi-wavelength data ranging from radio to high-energy γ rays (the latter being only upper limits). Unlike in Paper I where the γ-ray emission was modeled with the universal CR model in mind, here we use a spatial model that is directly inferred from the measurements of the giant radio halo as observed in radio and with Planck. We use six years of LAT exposure alongside with the deepest catalog to-date (3FGL) and its associated models for the foreground diffuse emission. We find faint residuals that are spatially coincident with parts of the radio halo and the radio source Coma A,

however much too faint to claim any detection or to further investigate its nature (for instance by investigating whether any of the excess displays signs of variability).

As a novelty, we use the bin-by-bin likelihood construction to derive spectrally independent constraints given our set of spatial templates. We then consider - for simplicity - various spectral indices on the resulting γ-ray spectrum and derive upper limits on the integrated γ-ray flux. We evaluate the overall sensitivity of the analysis by studying a large sample of blank fields and find it to be a factor few above the most favored remaining theoretical models in which the radio emission is generated by models where Cosmic Rays are confined by diffusion and reacceleration of secondaries by turbulence in the ICM.

7.2 Outlook

Prior to launch, it was widely expected that galaxy clusters would be established as γ-ray source class, yet even after six years of continued sky exposure the first firm detection is still pending.

Returning to DM, resulting constraints based on the non-observation γ rays will always be impacted by the irreducible backgrounds due to the inevitable CR-component, at least as long as the full virial volume of the cluster is considered. The contribution from CR physics is expected to be largest in the central region $R < R_{500}$, while the presence of substructure is most important towards the outskirts. However, outskirts are also the places were most relics are found, indicative of merger activity (see §4.3). In order to improve the purity of a DM-selected sample of clusters it is therefore necessary to select isolated nearby systems (likely cool-cores that show no signs of giant radio halos or relics) and focus on the outer parts for an analysis. At the same time improvements are expected due to the progress in regards to the understanding of DM substructure. As alluded to in §5.2.2 there is now a beginning consensus agreeing that a power-law extrapolation towards the smallest sub-halos is not supported by ΛCDM. As a result it becomes possible to provide more robust estimates on the boost factor, which are still uncertain up to a factor ~ 20 for cluster-size halos [M. Sánchez-Conde, private communication]. As a result, future constraints are expected to be more reliable but due to their comparatively large distance with respect to nearby dwarf galaxies, will remain substantially weaker for annihilating DM (at least up to WIMP masses of O(100GeV) for annihilation into $b\bar{b}$. Fig 7.1 shows the sensitivity to annihilating DM into $b\bar{b}$ from a simulation study of extended LAT exposure (10 years).We commented on the possibility of decaying DM in brief in this thesis which at present is less well explored. Since

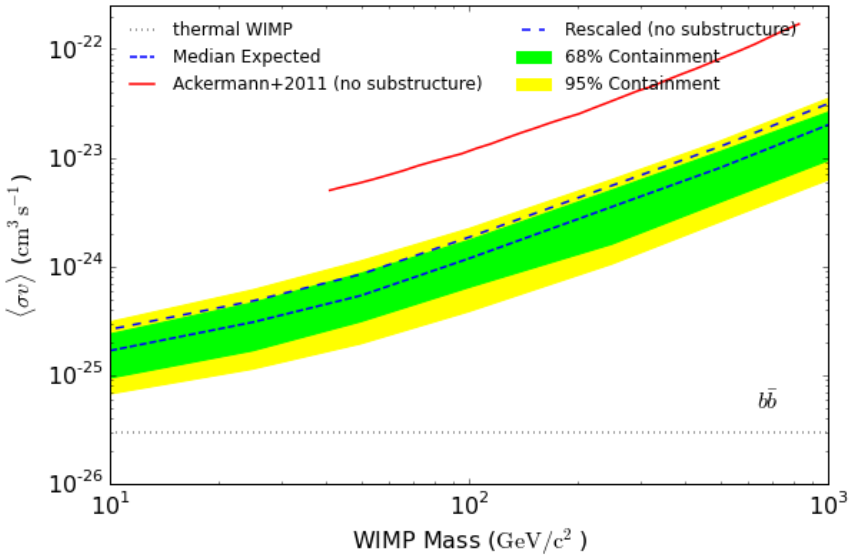

Figure 7.1. Predicted Sensitivity for WIMP annihilation into $b\bar{b}$ assuming the conservative boost factor setup described in this thesis. Shown as short-dashed (blue) line is the median expected upper limit on $\langle \sigma v \rangle$ for a sample of 32 of clusters that has been optimized towards maximizing the total predicted J-factor minimizing potential target overlap (c.f. §6.5). The green and yellow bands show the 68% and 95% containment bands (statistical uncertainties only). The red line is constructed by calculating the J-factor weighted average of the limits on $\langle \sigma v \rangle$ reported in the first LAT paper on clusters [13]. The long-dashed blue line corresponds to the median sensitivity but using the J-factors reported in Ackermann et al. [13]. The offset between both dashed lines can be used to gauge the importance of DM substructure. Finally, the gray-dotted line corresponds to the thermal WIMP annihilation cross section.

the J-factor scales linearly with the DM density, uncertainties have less impact and consequently the resulting limits may be robust if not competitive; an aspect which we plan to address in future works [work in preparation].

7.2.1 Detection Prospects with CTA

While there is little doubt that γ rays are expected from CR interactions, the biggest challenge in detecting this emission is due to the large uncertainty and poor constraints on the magnetic field strength and configuration in the ICM. Changes in either the configuration or the strength have immediate consequences on the predicted γ-ray fluxes, provided that one assumes that the radio-emitting CRes are of secondary origin [64], but as discussed before, direct measurements of the magnetic field are challenging. Future radio observations will thus be key in identifying potential other systems that can be studied to the same extent as the Coma cluster. The other difficulty when searching for the CR signature is that the emission is expected to be diffuse in nature. Here, ground based γ-ray telescopes, such as the upcoming Cherenkov Telescope Array (CTA) will provide a much better PSF compared to the LAT but their low energy threshold is significantly higher. CTA is envisioned to be an array consisting of different types of Cherenkov telescopes which in concert will observe the sky from $\sim 40\,\mathrm{GeV}$ to hundreds of TeV [92].

In Fig 7.2 we show the extrapolated sensitivity for our radio-inferred benchmark model studied in Paper IV given a LAT exposure of 10 years in contrast to a set of secondary models including the effect of turbulent re-acceleration in order to account for the details of the observed giant radio halo for the Coma cluster [67]. Also shown in the figure is the expected sensitivity of CTA based on an extrapolation of its point-source sensitivity. At the highest energies the expected γ-ray spectrum from CR interactions is expected to be power-law like with typical spectral indices comparable to that of the IGRB ($\Gamma \simeq 2.3$) which will make it hard to distinguish a cluster signal from this background.

In Doro et al. [85] the feasibility of detecting γ rays according to the predictions of the universal CR model (§5.1.1) was studied for different array configurations of CTA. For the Fornax cluster the 5σ detection threshold can be reached with O(1000) hours of continued observations. However, since we excluded the face-value model predictions in Paper I at more than 5σ it is safe to expect the required observation time to be at least a factor few higher. The other cluster studied in Doro et al. [85] is the Perseus cluster, which due to the strong emission from the two γ-ray sources IC310 and NGC1275 and its proximity to the Galactic plane is difficult to observe with the LAT. For this cluster the predictions of Pinzke et al. [137] are the most optimistic estimating that only ~ 100

hours of observation will be necessary to reach the 5σ detection limit. Correcting for the gained knowledge given the studies carried out in Paper I, a value of ~ 500 hours is however more likely.

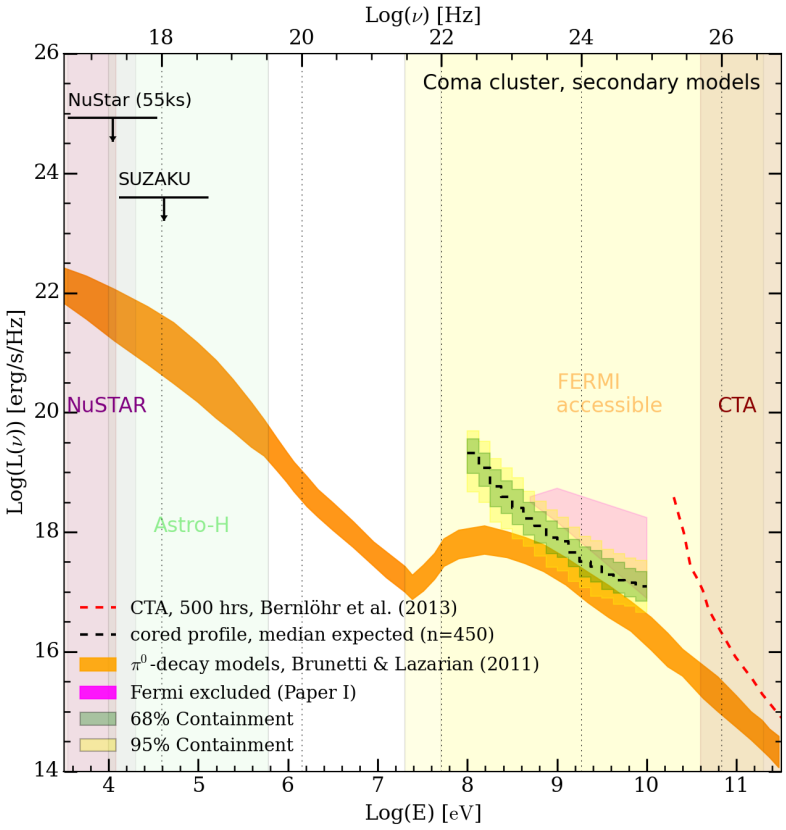

Figure 7.2. Shown as 'brazillian plot' in the energy range $100\,\mathrm{MeV} \leq E \leq 10\,\mathrm{GeV}$ is the extrapolated sensitivity of the analysis presented in Paper IV for a LAT exposure of 10 years in contrast with current models where radio emission arises from turbulent re-acceleration of secondary seed electrons (orange-colored band) [67]. The purple polygon denotes the conservative and optimistic limits reported in Paper I. Also shown as black markers are the various upper limits reported from X-ray observations [168; 95] along with an extrapolated sensitivity of the CTA array based on MC studies [53]. Note that the latter was taken to be the point-source sensitivity, rescaled to 500 hours of observation. The sensitivity for extended sources is expected to be weaker. The shaded areas represent the range of current and upcoming observatories, covering X-rays to TeV γ rays.

Svensk sammanfattning

Galaxhopar är universums största strukturer och de har bildats från en hierarkiskt uppbyggad av mindre strukturer såsom galaxer, grupper av galaxer osv. Det var observation av galaxer som rör sig snabbare än vad man förväntar sig från Newtons lag som den Svenska forskaren K. Lundmark [118] postulerade att något mycket mer massivt, den så kallade mörka materien, måste finnas inom en galaxhop för att skapa balansen i systemet.[1] även om vi vet att mörka materien finns i Universum (27% av universum är gjorda av mörk materie [27]), så är det helt oklar vad det egentligen är. En möjlighet är att det handlar om en helt ny elementarpartikel. *Weakly Interactive Massive Particles*, (WIMPar) är en bra kandidat för att bidra till mörka materien. Ifall den mörka materien är gjort av WIMPar då finns också möjligheten att två WIMPar kolliderar med varandra (i regioner där mörk materiens täthet är tillräckligt hög) och att vanliga partiklar skapas i dessa kollisioner.

Vi kan använder gammastrålning, alltså ljus som är flera tusentals mer energiska än ljusen vi kan se med våra ögon, för att kunna upptäcka ställen på himmeln där dessa WIMPar kolliderar. Detta är möjligt eftersom gammastrålar reser opåverkade av de olika magnetiska fält som finns emellan oss och objektet där det skapades. Samtidigt är galaxer syskon till vår egen galax, Vintergatan. Vi vet att det finns många laddade energetiska partiklar som rör sig inom Vintergatans egna magnetiska fält. När dessa partiklar kolliderar kan det också skapas gammastrålning, som därmed blir en förgrund för sökanden av WIMP kollisioner. Om man ser gammastrålning från galaxhopar måste man alltså försöka att skilja bort de astrofysikaliska gammastrålarna från de som skulle kunna ha kommit från mörka materiens kollisioner.

I denna avhandlingen berättar vi hur Fermi teleskopet kan användas för att upptäcka gammastrålning från galaxhopar, som man hade tänkt skulle kunna vara ljusstarka innan Fermi började. Vi befinner oss nu i sjunde året av experimentens livstid och än så länge har vi inte sätt någon gammastrålning från hopar, eller kluster (förutom gammastrålning som troligtvis skapades i en radiogalax inom en del av de kluster som vi analyserat). Därför berättar vi i avhandlingen om hur man kan använda statistiska tekniker för att få fram så mycket information så möjligt och hur detta kan används för att begränsa den fysikaliska friheten hos de processer där gammastrålning produceras (t.ex. acceleration

[1] Ett par år senare observerade F. Zwicky Coma klustret [174] och kom fram till samma slutsats och han är idag associerade med upptäckning av mörka materien tillsammans med Vera Rubin, fast betydligt senare [144].

av laddade partiklar genom chockvågor eller från annihilationen av de så kallade WIMP mörk materie partiklar).

Vi använder en statistiskt teknik där vi kombinerar olika observationer, genom at 'stapla' ihop de individuella sannolikheterna och maximera resultatet. Genom att göra detta kom vi fram till att antingen är processen där kosmisk strålning, eller mer exakt de kosmiska protoner som får energi genom chockvågor via uppstår under uppbyggandet av strukturer, är inte lika effektivt som man hade tänkt tidigare eller att det finns betydligt mindre kosmiska protoner i en galax kluster än vad man har kommit fram till från observationen av gas i galaxhopar.

Virgo är galaxhop-grannen som ligger närmst oss, med på ett avstånd av 'bara' 20 megaparsec (ungefär 600 gånger större än Vintergatans diameter). Vi hittade ett överskott av gammastrålning i riktning av klustret som dock kan förklaras med att variera förgrundsmodellen, alltså komponenten som modellerar Vintergatans egen gammastrålning och gammastålningskällor som Fermi ser (en detaljerat modell behövs för att kunna observera galaxhopar som ligger utanför vår egna galax). Eftersom vi inte sett gammastrålning från kluster kan vi härleda gränser på annileringstvärsnitt för WIMPar till gammastrålning samt andra astrofysikaliska processer där gammastrålning kan produceras i klustret.

Vi har också undersökt Coma klustret, alltså den galaxhop som observerades tidigt av Zwicky och vi såg först ett överskott av strålning från detta kluster, som efter en närmare undersökning kan dock förklaras som en statistiskt fluktuation. Slutligen letar vi även efter monokromatiska gammastrålning, alltså linjer i spektrumet. De kan bara komma från exotisk fysik, t.ex. från annihilation av mörk materie partiklar (eller deras sönderfall) och är därför en så kallat 'smoking gun' signatur, som inte kan ha ett konventionellt astrofysikaliskt ursprung. Vi hittar inga linjer och får fram gränser som är mindre begränsande än de från observationen av Vintergatans centrum med Fermi teleskopet.

På slutet kommenterar vi även om perspektiven att upptäcka gammastrålningen från galaxhopar med framtidens nästa stora gammastrålningsexperiment, den så kallade Cherenkov Telescope Array.

Bibliography

[1] Abdo, A. A., et al. 2009, Science, 325, 848

[2] —. 2009, ApJ, 699, 31

[3] —. 2009, ApJ, 707, 55

[4] —. 2010, A&A, 523, A46

[5] —. 2010, Science, 328, 725

[6] —. 2010, ApJS, 188, 405

[7] —. 2010, Physical Review Letters, 104, 091302

[8] —. 2010, A&A, 512, A7

[9] —. 2010, Physical Review Letters, 104, 101101

[10] Acero, F., et al. 2015, ApJS, 218, 41

[11] Ackermann, M., et al. 2012, ApJ, 750, 3

[12] Ackermann, M., et al. 2014, ApJ, 793, 64

[13] Ackermann, M., et al. 2010, J. Cosmology Astropart. Phys., 5, 25

[14] Ackermann, M., et al. 2011, Physical Review Letters, 107, 241302

[15] Ackermann, M., et al. 2012, ApJ, 755, 164

[16] —. 2012, Physical Review Letters, 108, 011103

[17] Ackermann, M., et al. 2012, ApJS, 203, 4

[18] Ackermann, M., et al. 2013, Science, 339, 807

[19] —. 2013, ApJ, 765, 54

[20] Ackermann, M., et al. 2013, Phys. Rev. D, 88, 1305.5597

[21] Ackermann, M., et al. 2013, ApJS, 209, 34

[22] Ackermann, M., et al. 2014, Phys. Rev. D, 89, 042001

[23] Ackermann, M., et al. 2014, Physical Review Letters, 112, 151103

[24] —. 2015, ApJ, 799, 86

[25] —. 2015, ArXiv e-prints, arXiv:1506.00013 [astro-ph.HE]

[26] Ade, P. A. R., et al. 2014, A&A, 571, A16

[27] Ade, P. A. R., et al. 2015, ArXiv e-prints, arXiv:1502.01589

[28] Adriani, O., et al. 2009, Nature, 458, 607

[29] —. 2011, Science, 332, 69

[30] Aguilar, M., et al. 2013, Physical Review Letters, 110, 141102

[31] Aharonian, F., et al. 2008, Reports on Progress in Physics, 71, 096901

[32] Aharonian, F., Khangulyan, D., & Malyshev, D. 2012, A&A, 547, A114

[33] Aharonian, F., et al. 2006, A&A, 457, 899

[34] Aharonian, F., et al. 2009, ApJ, 695, L40

[35] Ajello, M., et al. 2015, ArXiv e-prints, arXiv:1503.02664 [astro-ph.HE]

[36] Ajello, M., et al. 2015, ApJ, 800, L27

[37] Akamatsu, H., et al. 2012, PASJ, 64, 67

[38] Aleksić, J., et al. 2010, ApJ, 723, L207

[39] Aleksić, J., et al. 2012, A&A, 539, L2

[40] Aliu, E., et al. 2011, Science, 334, 69

[41] Anderson, B., et al. 2015, ArXiv e-prints, arXiv:1502.03081 [astro-ph.HE]

[42] Arrabito, L., et al. 2014, INFN-CNAF Annual Report 2013, ed. F. G. Luca dell'Agnello & C. Grandi (CNAF), 46

[43] Arrabito, L., et al. 2014, Journal of Physics Conference Series, 513, 032003

[44] Askew, A., et al. 2014, International Journal of Modern Physics A, 29, 30041

[45] Atwood, W., et al. 2013, ArXiv e-prints, arXiv:1303.3514 [astro-ph.IM]

[46] Atwood, W. B., & GLAST Collaboration. 1994, Nuclear Instruments and Methods in Physics Research A, 342, 302

[47] Atwood, W. B., et al. 2007, Astroparticle Physics, 28, 422

[48] Atwood, W. B., et al. 2009, ApJ, 697, 1071

[49] Bartlett, M. S. 1953, Biometrika, 40, pp. 306

[50] Baudis, L. 2012, Physics of the Dark Universe, 1, 94

[51] Berezinsky, V. S., Blasi, P., & Ptuskin, V. S. 1997, ApJ, 487, 529

[52] Bergström, L., & Goobar, A. 2004, Cosmology and Particle Astrophysics (Springer), p. 185

[53] Bernlöhr, K., et al. 2013, Astroparticle Physics, 43, 171

[54] Bissaldi, E., et al. 2009, Experimental Astronomy, 24, 47

[55] Blasi, P., Gabici, S., & Brunetti, G. 2007, International Journal of Modern Physics A, 22, 681

[56] Blumenthal, G. R., & Gould, R. J. 1970, Reviews of Modern Physics, 42, 237

[57] Boinee, P., et al. 2003, in Science with the New Generation of High Energy Gamma-Ray Experiments : Between Astrophysics and Astroparticle Physics, ed. S. Ciprini, A. de Angelis, P. Lubrano, & O. Mansutti, 141

[58] Bonafede, A., et al. 2010, A&A, 513, A30

[59] Boyarsky, A., Malyshev, D., & Ruchayskiy, O. 2013, Physics of the Dark Universe, 2, 90

[60] Bregeon, J., Charles, E., & for the Fermi-LAT collaboration, M. W. 2013, 1304.5456

[61] Bringmann, T., & Weniger, C. 2012, Physics of the Dark Universe, 1, 194

[62] Brown, S., & Rudnick, L. 2011, MNRAS, 412, 2

[63] Bruel, P., & Fermi-LAT Collaboration. 2012, Journal of Physics Conference Series, 404, 012033

[64] Brunetti, G., et al. 2012, MNRAS, 426, 956

[65] Brunetti, G., et al. 2009, A&A, 507, 661

[66] Brunetti, G., & Jones, T. W. 2014, International Journal of Modern Physics D, 23, 30007

[67] Brunetti, G., & Lazarian, A. 2007, MNRAS, 378, 245

[68] —. 2011, MNRAS, 410, 127

[69] Brunetti, G., et al. 2001, MNRAS, 320, 365

[70] Carlson, P., et al. 1996, Nuclear Instruments and Methods in Physics Research A, 376, 271

[71] Casandjian, J.-M., & for the Fermi Large Area Telescope Collaboration. 2015, ArXiv e-prints, arXiv:1502.07210 [astro-ph.HE]

[72] Casandjian, J.-M., Grenier, I., & for the Fermi Large Area Telescope Collaboration. 2009, arXiv:0912.3478, arXiv:0912.3478 [astro-ph.HE]

[73] Cassano, R., et al. 2010, A&A, 509, A68

[74] Charles, E., & Fermi LAT Collaboration. 2012, in American Astronomical Society Meeting Abstracts, Vol. 219, American Astronomical Society Meeting Abstracts #219, #149.15

[75] Chen, Y., et al. 2007, A&A, 466, 805

[76] Chernoff, H. 1952, The Annals of Mathematical Statistics, 23, 493

[77] Clark, G. W., Garmire, G. P., & Kraushaar, W. L. 1968, ApJ, 153, L203

[78] Conrad, J. 2014, ArXiv e-prints, arXiv:1411.1925 [hep-ph]

[79] Crocker, R. M., et al. 2015, ApJ, 808, 107

[80] de Palma, F., Brandt, T. J., Johannesson, G., & others for the Fermi-LAT collaboration. 2013, Proc. of the 2012 Fermi Symposium - eConf Proceedings C121028, arXiv:1304.1395 [astro-ph.HE]

[81] Delahaye, T., et al. 2011, A&A, 531, A37

[82] Dennison, B. 1980, ApJ, 239, L93

[83] Dolag, K., & Ensslin, T. A. 2000, A&A, 362:151, astro-ph/0008333

[84] Donnert, J., et al. 2010, MNRAS, 401, 47

[85] Doro, M., et al. 2013, Astroparticle Physics, 43, 189

[86] Drlica-Wagner, A. 2013, Doctoral thesis, Stanford University

[87] Dutson, K. L., et al. 2013, MNRAS, 429, 2069

[88] Espinoza, C. M., et al. 2013, MNRAS, 430, 571

[89] Ettori, S., & Fabian, A. C. 1999, MNRAS, 305, 834

[90] Fichtel, C. E., et al. 1975, ApJ, 198, 163

[91] Fichtel, C. E., Simpson, G. A., & Thompson, D. J. 1978, ApJ, 222, 833

[92] Funk, S., Hinton, J. A., & CTA Consortium. 2013, Astroparticle Physics, 43, 348

[93] Gao, L., et al. 2012, MNRAS, 419, 1721

[94] Gao, L., et al. 2012, MNRAS, 425, 2169

[95] Gastaldello, F., et al. 2015, ApJ, 800, 139

[96] Giacintucci, S., et al. 2009, A&A, 505, 45

[97] Graham, M. L., et al. 2012, ApJ, 753, 68

[98] Green, A. M., Hofmann, S., & Schwarz, D. J. 2004, MNRAS, 353, L23

[99] Han, J., et al. 2012, MNRAS, 427, 1651

[100] Hayashida, M., et al. 2013, ApJ, 779, 131

[101] Hektor, A., Raidal, M., & Tempel, E. 2013, ApJ, 762, L22

[102] Helder, E. A., et al. 2009, Science, 325, 719

[103] Hoecker, A., et al. 2007, ArXiv Physics e-prints, physics/0703039

[104] Hudson, D. S., et al. 2010, A&A, 513, A37

[105] James, F., & Roos, M. 1975, Comput. Phys. Commun., 10, 343

[106] Jeltema, T. E., & Profumo, S. 2008, J. Cosmology Astropart. Phys., 2008, 003

[107] Kargaltsev, O., Pavlov, G. G., & Garmire, G. P. 2006, ApJ, 646, 1139

[108] Kirsch, M. G. F., et al. 2004, in Society of Photo-Optical Instrumentation Engineers (SPIE) Conference Series, Vol. 5488, UV and Gamma-Ray Space Telescope Systems, ed. G. Hasinger & M. J. L. Turner, 103

[109] Kolmogorov, A. 1941, Akademiia Nauk SSSR Doklady, 30, 301

[110] Kraushaar, W. L., et al. 1972, ApJ, 177, 341

[111] Kravtsov, A. V., Vikhlinin, A., & Nagai, D. 2006, ApJ, 650, 128

[112] Kushnir, D., & Waxman, E. 2009, J. Cosmology Astropart. Phys., 8, 2

[113] Kuss, M., et al. 2015, The Fermi-LAT experiment at the INFN CNAF Tier 1, ed. F. G. Luca dell'Agnello & C. Grandi

[114] Lande, J., et al. 2012, ApJ, 756, 5

[115] Leitherer, C. 2000, EUROPEAN SPACE AGENCY-PUBLICATIONS-ESA SP, 445, 37

[116] Longair, M. S. 2011, High Energy Astrophysics (Cambridge University Press)

[117] Longo, F., et al. 2006, in Frontiers of Fundamental and Computational Physics, ed. B. G. Sidharth, F. Honsell, & A. de Angelis, 309

[118] Lundmark, K. 1930, Meddelanden från Lunds Observatorium, 125, 10

[119] Macías-Ramírez, O., et al. 2012, Phys. Rev. D, 86, 076004

[120] Mattox, J. R., et al. 1996, ApJ, 461, 396

[121] Mavromanolakis, G. 2004, ArXiv Physics e-prints, physics/0409039

[122] McEnery, J. E., Fermi-LAT Collaboration, & Fermi-GBM Team. 2014, in American Astronomical Society Meeting Abstracts, Vol. 223, American Astronomical Society Meeting Abstracts #223

[123] Meegan, C., et al. 2009, ApJ, 702, 791

[124] Mohr, J. J., Mathiesen, B., & Evrard, A. E. 1999, ApJ, 517, 627

[125] Moiseev, A. A., et al. 2007, Astroparticle Physics, 27, 339

[126] Nagai, D., Vikhlinin, A., & Kravtsov, A. V. 2007, ApJ, 655, 98

[127] Navarro, J. F., Frenk, C. S., & White, S. D. M. 1995, MNRAS, 275:720-740,1995, astro-ph/9408069

[128] Navarro, J. F., Frenk, C. S., & White, S. D. M. 1996, ApJ, 462, 563

[129] Neronov, A., Semikoz, D., & Vovk, I. 2010, A&A, 519, L6

[130] Nolan, P. L., et al. 2012, ApJS, 199, 31

[131] Norbury, J. W. 2009, Nuclear Instruments and Methods in Physics Research B, 267, 1209

[132] Olive, K. A., & Particle Data Group. 2014, Chinese Physics C, 38, 090001

[133] Piffaretti, R., & Valdarnini, R. 2008, A&A, 491, 71

[134] Pinzke, A., Oh, S. P., & Pfrommer, C. 2015, ArXiv e-prints, arXiv:1503.07870 [astro-ph.HE]

[135] Pinzke, A., & Pfrommer, C. 2010, MNRAS, 409, 449

[136] Pinzke, A., Pfrommer, C., & Bergström, L. 2009, Physical Review Letters, 103, 181302

[137] —. 2011, Phys. Rev. D, 84, 123509

[138] Prada, F., et al. 2012, MNRAS, 423, 3018

[139] Profumo, S., Sigurdson, K., & Kamionkowski, M. 2006, Physical Review Letters, 97, 031301

[140] Prokhorov, D. A., & Churazov, E. M. 2014, A&A, 567, A93

[141] Read, A. M., et al. 2011, A&A, 534, A34

[142] Reiprich, T. H., & Böhringer, H. 2002, ApJ, 567, 716

[143] Rolke, W. A., López, A. M., & Conrad, J. 2005, Nuclear Instruments and Methods in Physics Research A, 551, 493

[144] Rubin, V. C., & Ford, Jr., W. K. 1970, ApJ, 159, 379

[145] Rubin, V. C., Ford, W. K. J., & . Thonnard, N. 1980, ApJ, 238, 471

[146] Sánchez-Conde, M. A., & Prada, F. 2014, MNRAS, 442, 2271

[147] Schlickeiser, R., Sievers, A., & Thiemann, H. 1987, A&A, 182, 21

[148] Sgrò, C. 2014, in Astroparticle, Particle, Space Physics and Detectors for Physics Applications - Proceedings of the 14th ICATPP Conference, ed. S. Giani & et al., 125

[149] Sijbring, L. G. 1993, A radio continuum and HI line study of the perseus cluster

[150] Sreekumar, P., et al. 1994, ApJ, 426, 105

[151] Stappers, B. W., et al. 2003, Science, 299, 1372

[152] Strong, A. W., & Bignami, G. F. 1983, ApJ, 274, 549

[153] Strong, A. W., Moskalenko, I. V., & Ptuskin, V. S. 2007, Annual Review of Nuclear and Particle Science, 57, 285

[154] Su, M., & Finkbeiner, D. P. 2012, ArXiv e-prints, arXiv:1206.1616 [astro-ph.HE]

[155] Su, M., Slatyer, T. R., & Finkbeiner, D. P. 2010, ApJ, 724, 1044

[156] Takahashi, M., et al. 2015, ArXiv e-prints, arXiv:1503.01364 [astro-ph.HE]

[157] Tanaka, Y., Inoue, H., & Holt, S. S. 1994, PASJ, 46, L37

[158] Tempel, E., Hektor, A., & Raidal, M. 2012, J. Cosmology Astropart. Phys., 9, 32

[159] Thierbach, M., Klein, U., & Wielebinski, R. 2003, A&A, 397, 53

[160] Thompson, D. J., et al. 1993, ApJS, 86, 629

[161] Ukwatta, T. N., et al. 2010, ArXiv e-prints, arXiv:1003.4515 [astro-ph.HE]

[162] van Weeren, R. J., Röttgering, H. J. A., Brüggen, M., & Hoeft, M. 2010, Science, 330, 347

[163] van Weeren, R. J., Intema, H. T., Lal, D. V., et al. 2014, ApJ, 786, L17

[164] Vladimirov, A. E., et al. 2011, Computer Physics Communications, 182, 1156

[165] Völk, H. J., Aharonian, F. A., & Breitschwerdt, D. 1996, Space Sci. Rev., 75, 279

[166] Weniger, C. 2012, J. Cosmology Astropart. Phys., 8, 7

[167] Weniger, C., et al. 2013, ArXiv e-prints, arXiv:1305.4710 [astro-ph.HE]

[168] Wik, D. R., et al. 2009, ApJ, 696, 1700

[169] Wilks, S. S. 1938, The Annals of Mathematical Statistics, 9, pp. 60

[170] Xu, Y., et al. 2015, ApJ, 801, 105

[171] Zandanel, F., et al. 2015, A&A, 578, A32

[172] Zimmer, S. 2013, Searching for Gamma Rays from Galaxy Clusters with the Fermi Large Area Telescope - Cosmic Rays and Dark Matter, Licenciate Thesis, Department of Physics, Stockholm University `http://www.diva-portal.org/smash/get/diva2:665822/FULLTEXT01.pdf`

[173] Zimmer, S., et al. 2012, Journal of Physics Conference Series, 396, 032121

[174] Zwicky, F. 1933, Helvetica Physica Acta, 6, 110